Chemical and Biological Technologies in Agriculture

RESEARCH

Open Access

Engineering myxinidin-based supramolecular architectures for advanced antifungal applications in food protection

Simone Braccia[1†], Rosa Bellavita[1†], Oluwasegun Eric Ajayi[1,2], Marta Ranesi[3], Lorenzo Emiliano Imbò[3], Luca De Stefano[4], David Turrà[3,5,6,7], Rosarita Tatè[8], Camilla Casciello[9], Principia Dardano[4], Stefania Vitale[3,5*], Annarita Falanga[3*] and Stefania Galdiero[1*]

Abstract

Background The antimicrobial peptide WMR-4, a myxinidin-derived sequence with Aib and D-amino acid substitutions, showed enhanced stability and strong antifungal activity against *Fusarium oxysporum* in vitro.

Results Biophysical studies indicated a lytic mechanism via deep membrane insertion and leakage. However, free WMR-4 failed to block fungal penetration through cellulose barriers, revealing limits in complex systems. To overcome this, we developed supramolecular nanofibers functionalized with WMR-4 and the cell-penetrating peptide gH625. These nanofibers inhibited germ tube formation, partially reduced cellulose membrane penetration, and provided enhanced protection in biological contexts. Specifically, nanofibers limited opportunistic saprophytic colonization in apple tissues lacking epidermal barriers while preserving tissue integrity in intact tomato models, demonstrating barrier-specific therapeutic protection. SEM and AFM confirmed stable nanoscale coatings integrated into plant epidermal layers.

Conclusions These results highlight WMR-4 as a potent antifungal candidate and demonstrate the potential of AMP-functionalized supramolecular nanostructures for agricultural applications.

Keywords Nanofibers, *Fusarium oxysporum*, Tomato fruits, Drug delivery

[†]Simone Braccia and Rosa Bellavita have contributed equally to this work.

*Correspondence:
Stefania Vitale
stefania.vitale@unina.it
Annarita Falanga
annarita.falanga@unina.it
Stefania Galdiero
stefania.galdiero@unina.it
Full list of author information is available at the end of the article

Graphical abstract

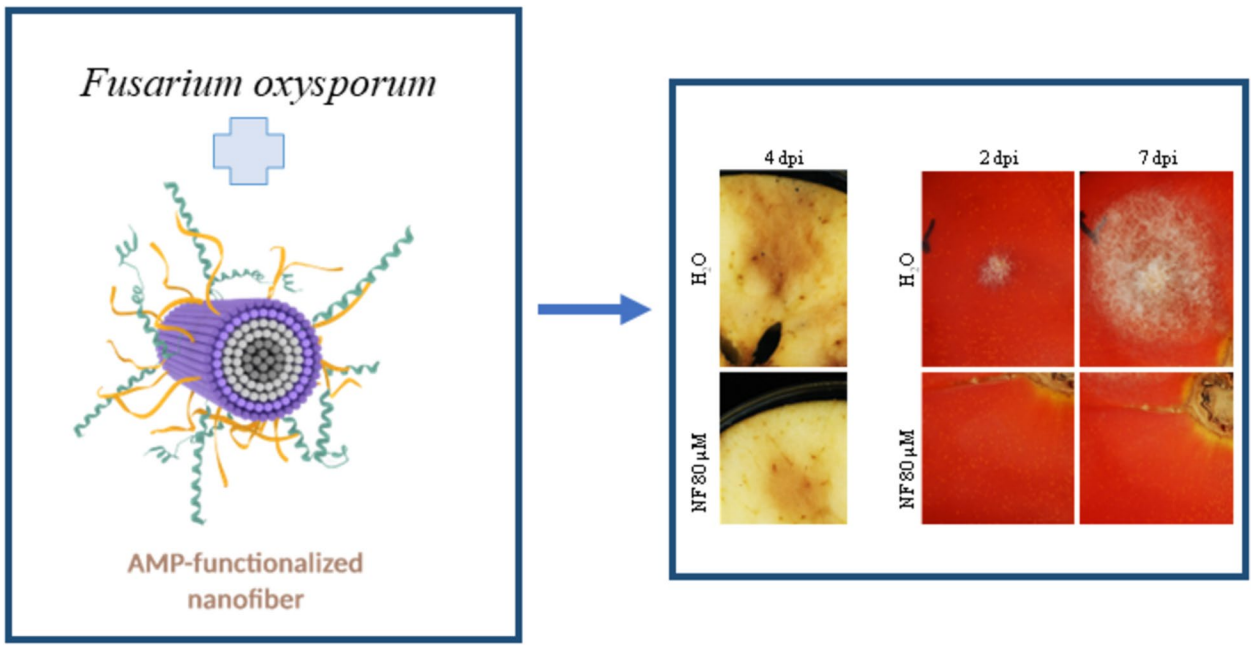

Background

The widespread misuse of conventional antibiotics in both human and veterinary medicine has accelerated the emergence of antimicrobial resistance, now recognized as a critical global health threat [1–3]. In parallel, the emergence of antimicrobial resistance represents a critical issue also in agriculture, with fungal phytopathogens causing over $220 billion in global crop losses annually while simultaneously threatening immunocompromised patients as opportunistic pathogens [4–6]. Furthermore, the Food and Agriculture Organization estimates that plant diseases determine a 20–40% of crop production loss because of pests and pathogens [7–11].

Among fungal pathogens, *Fusarium oxysporum* exemplifies this multifaceted challenge through its remarkable adaptability and broad host range [12, 13]. This ubiquitous, soil-borne fungus represents one of the most economically devastating plant pathogens worldwide, capable of infecting over 100 plant species as a result of its diverse *formae speciales* (*f. sp.*), each genetically adapted, through specialized virulence mechanisms, to a specific host [14–17]. The pathogen's impact extends across economically critical crops including melon, tomato, cotton, and banana, with some strains causing complete crop failures in susceptible cultivars [18–20]. Beyond pre-harvest losses, *Fusarium* species significantly impact also post-harvest food security by accelerating tissue softening and promoting rapid maceration in fresh produce during storage and transport under both temperate and tropical conditions [21–24]. The ability to thrive under high humidity and nutrient-rich conditions drastically reduces storage time and increases postharvest losses during transport and retail distribution, directly impacting global food supply chains. Current agricultural management of *F. oxysporum* infections relies on synthetic fungicides including triazoles, strobilurins, and copper-based compounds, with triazoles demonstrating superior efficacy across formae speciales with EC50 values below 0.5 µg/mL [25]. However, these approaches face critical limitations including resistance development through novel mechanisms such as Type I myosin FoMyo5 mutations and CYP51A gene alterations conferring 100-fold resistance increases [26, 27] environmental persistence concerns leading to potential regulatory restrictions [28, 29], and variable efficacy across different *formae speciales* where identical fungicides exhibit dramatically different effectiveness against subspecies [30]. Biological control strategies using *Trichoderma* spp. show promise in laboratory conditions but demonstrate inconsistent field performance due to environmental variability and complex soil-pathogen interactions [31, 32], underscoring the urgent need for innovative antimicrobial approaches that circumvent conventional

resistance mechanisms while providing sustainable protection across diverse agricultural systems and *formae speciales*.

Besides the agricultural concern, *F. oxysporum* has emerged as a clinically significant opportunistic pathogen in immunocompromised humans, particularly affecting patients with haematological malignancies, transplant recipients, and individuals with acquired immunodeficiency syndromes [33]. Clinical isolates demonstrate considerable genetic diversity and have been associated with nosocomial outbreaks, highlighting the pathogen's adaptability to healthcare environments and its potential for horizontal gene transfer [34–37]. The mortality rates associated with invasive *F. oxysporum* infections in immunocompromised patients can exceed 80% [37], emphasizing the urgent need for effective innovative antimicrobial strategies that can address both agricultural and medical applications [38, 39].

Antimicrobial peptides (AMPs) represent a particularly promising class of bioactive molecules found in plants and animals that exert their action through direct membrane disruption and multitarget interactions [40–43], offering sustainable alternatives to synthetic fungicides and conventional antifungal agents, likely circumventing conventional resistance mechanisms [44, 45]. To overcome the inherent limitations of natural AMPs, diverse chemical modifications have been developed including the D-amino acid substitution, lipidation, PEGylation, glycosylation, cyclization, as well as stapling [46–48]. In this scenario, advanced materials and micro/nanotechnologies based on AMPs' delivery also offer promising avenues for combating resistant fungal infections, particularly in agricultural settings where conventional treatments are increasingly ineffective [49–51]

Herein, we selected myxinidin, a marine peptide derived from the epidermal mucus of the hagfish (*Myxine glutinosa* L.), which exhibits a unique combination of broad-spectrum antimicrobial activity, membrane-active properties, and minimal cytotoxicity toward human cells [52]. The peptide's natural origin and evolutionary optimization for antimicrobial defense in marine environments provide a robust foundation for biotechnological applications. Building on this foundation, our laboratory developed WMR (NH_2-WGIRRILKYGKRSK-$CONH_2$), a rationally designed Myxinidin variant which demonstrates enhanced antibacterial efficacy against both Gram-positive and Gram-negative bacteria [52]. Compared to the native peptide, WMR features an additional tryptophan at the N-terminus, likely contributing to its potent membrane-disruptive capabilities, and a higher content of positively charged residues (arginines) [52]. To further improve proteolytic stability, we designed an analogue, WMR-4, in which Gly^2 is replaced with the unnatural amino acid 2-aminoisobutyric acid (Aib), and Ser^{13} and Lys^{14} are substituted with their D-enantiomers. WMR-4 exhibited markedly improved stability in serum over WMR [53]. Additionally, we previously developed nanofibers functionalized with WMR at their periphery [54], which effectively inhibited biofilm formation and eradicated established biofilms of *Pseudomonas aeruginosa* (Gram-negative) and *Candida albicans* [55]. These findings support the continued development of WMR-4 as a promising AMP for combating fungal pathogens present in agricultural settings.

To address this challenge, we initially assessed the antifungal properties of WMR-4 against liquid cultures of *F. oxysporum*, focusing on its eventual capacity to block fungal penetration through cellulose-based membranes. Furthermore, we focussed on the need for a suitable delivery system to enhance its protective effectiveness in more complex environments [56].

We previously aimed at self-assembling materials as a strategy to develop antimicrobial agents with enhanced proteolytic stability and improved antifungal efficacy [54, 57]. In fact, by harnessing dynamic, reversible non-covalent interactions, antimicrobial materials can be engineered at the molecular level through controlled supramolecular assembly [58]. Notably, the multivalent display of AMPs on the surface of self-assembled nanostructures offers a promising approach for improving their therapeutic performance compared to single soluble peptides, by enhancing their stability while augmenting and controlling the local concentration of the active peptides, which enables their enhanced interactions with microbes.

Building on this, we developed a self-assembled nanosystem with WMR-4 displayed on its surface, exploiting the spontaneous organization of molecules into ordered structures through supramolecular interactions. Our design employs peptide amphiphiles (PAs), where the balance between hydrophobic and hydrophilic domains governs self-assembly, enabling the formation of nanostructures with tunable and well-defined properties.

Furthermore, this modular platform allows for the incorporation of other functional motifs to create multifunctional materials suitable for more complex matrices such as food systems, particularly those with protective barriers covering fruits and vegetables. Thus, to further enhance the antifungal potential and improve the ability to cross these barriers, we functionalized the surface of the nanostructure with a cell-penetrating peptide (CPP) developed in our lab, gH625 [59]. This CPP is known for its ability to transport a wide range of molecular cargos across membranes and is likely to enhance antifungal efficacy on plant surfaces by facilitating intracellular delivery and inhibiting fungal growth [60].

The activity of the developed self-assembled WMR-4-based nanofibers (NFs) was evaluated both in vitro and in vivo using apple and tomato models, demonstrating that the system is effective not only in highly vulnerable tissues lacking protective barriers but also in the presence of barriers, such as in tomatoes.

Our nanosystem represents a promising strategy for designing smart materials that can be applied to protect agricultural products from fungal attack. By modifying the AMP, it is possible to tailor the system against different fungal and/or bacterial pathogens.

Materials and method

Materials

N^{α} -Fmoc-protected amino acids were obtained from GL Biochem Ltd. (Shanghai, China). Rink amide p-methylbenzhydrylamine (MBHA) resin, Fmoc-Lys(Mtt), Fmoc-D-Ser(tBu)-OH, Fmoc-D-Lys(Boc)-OH, Fmoc-Aib-OH, Fmoc-O2Oc-OH, piperidine, ergosterol, trifluoroacetic acid (TFA), Oxyma pure, and 1-[bis (dimethylamino) methylene]-1H-1,2,3-triazolo[4,5-b]pyridinium 3-oxid hexafluorophosphate (HATU) were acquired from Iris-Biotec GmbH. 1,1,1,3,3,3-Hexafluoro-2-propanol (HFIP), solvents such as *N,N*-dimethylformamide (DMF), dichloromethane (DCM), and chloroform, nonadecanoic acid (C19), *N,N'*-diisopropylcarbodiimide (DIC), triisopropylsilane (TIS),, Nile Red, Thioflavin T, and *N,N*-diisopropylethylamine (DIEA) were purchased by Merck (Milan, Italy). Phospholipids: 1-palmitoyl-2-oleoyl-*sn*-glycero-3-phosphocholine (POPC), 1-palmitoyl-2-oleoyl-sn-glycero-3-phosphoethanolamine (POPE), phosphatidylserine (PS), Phosphatidylinositol (PI), Rhodamine and 12-(N-methyl-N-(7-nitrobenz-2-oxa-1,3-diazol-4-yl)) (NBD)–phosphatidylethanolamine (Rho-PE and NBD-PE, respectively), were purchased from Avanti Polar Lipids (Birmingham, AL, USA).

Peptide synthesis

WMR-4 and the peptides P1, P2, P3, and P2-a were synthesized on Rink Amide resin (loading capacity: 0.63 mmol/g) via standard solid-phase Fmoc (9-fluorenylmethoxycarbonyl) chemistry (Table 1) [61].

For the peptides P1, P2, P3 and P2-a, Fmoc-Lys (Mtt)-OH was employed as the first amino acid to allow selective conjugation of nonadecanoic acid (C19) on the lysine side-chain.

During the elongation of the peptide sequence each Fmoc deprotection was performed by treatment with 30% piperidine in DMF (2 × 10 min), while the coupling reaction was carried out through two steps: (i) Fmoc-protected amino acid (2 equiv), DIC, 2 equiv) and Oxyma pure (2 equiv) in DMF for 40 min; (ii) Fmoc-amino acid (2 equiv), HATU (2 equiv), and DIPEA (4 equiv) in DMF for 40 min.

For the C19 conjugation, Mtt protecting group from the lysine side chain was performed by repeated treatments (15 cycles) of the resin with a cleavage cocktail composed of DCM:TFA:TIS (94:1:5, *v/v/v*) [49]. Completion of deprotection was verified via the colorimetric Kaiser test, which detects free primary amines on the solid support. The lipid conjugation was achieved using C19 (2 equiv), DIC (2 equiv), and Oxyma pure (2 equiv) in NMP, followed by a second coupling step using HATU (2 equiv) and DIPEA (4 equiv) in NMP for 2 h. Peptides were cleaved from the resin using a mixture of TFA/H_2O/TIS (95:2.5:2.5, *v/v/v*) under agitation for 3 h. After cleavage, peptides were precipitated by addition of cold diethyl ether and collected by centrifugation (2 cycles, 15 min each at 6000 rpm). For the purification, WMR-4 crude was dissolved with 10% of acetonitrile in water, while crude self-assembled peptides were dissolved in a solution of 10% HFIP and 0.1% TFA in water. The purification was performed using semi-preparative reversed-phase HPLC and Phenomenex Kinetex C18 column (5 µm, 100 Å, 150 × 21.2 mm). Elution was performed with a linear gradient of solvent B (0.1% TFA in acetonitrile) in solvent A (0.1% TFA in water) from 10 to 90% over 20 min at a flow rate of 15 mL/min, with UV detection at 220 nm. The identity of all peptides was confirmed by electrospray ionization mass spectrometry (ESI–MS), while the purity was checked by analytical HPLC on a Phenomenex Jupiter 4u Proteo column (90 Å, 150 × 4.6 mm) (*see supporting information*, Figure S1–S5).

Table 1 Sequence of peptides WMRK-4, P1, P2, P3 and WMR4-P2

Short name	Peptide	Sequence
WMR-4	WMR-4	NH_2-Trp-Aib-Ile-Arg-Arg-Ile-Leu-Lys-Tyr-Gly-Lys-Arg-DSer-DLys- $CONH_2$
P1		NH_2-Gly-Asp-Asp-Ser-Ala-Ala-Ala-Ala-Ala-Ala-Lys(C19)-$CONH_2$
P2		NH_2-Gly-Lys-Arg-Ser-Ala-Ala-Ala-Ala-Ala-Ala-Lys(C19)-$CONH_2$
P3	gH-P2	NH_2-His-Gly-Leu-Ala-Ser-Thr-Leu-Thr-Arg-Ala-Trp-Ala-His-Tyr-Asn-Ala-Leu-Ile-Arg-Ala-Phe-Gly-Lys-Arg-Ser-Ala-Ala-Ala-Ala-Ala-Ala-Lys(C19)-$CONH_2$
P2-a	WMR-4-P2	NH_2-Trp-Aib-Ile-Arg-Arg-Ile-Leu-Lys-Tyr-Gly-Lys-Arg-DSer-DLys-PEG2- Gly-Lys-Arg-Ser-Ala-Ala-Ala-Ala-Ala-Ala-Lys(C19)-$CONH_2$

In vitro and in vivo antifungal evaluation against Fusarium oxysporum fungal strain and culture conditions

The tomato pathogenic isolate *Fusarium oxysporum* f. sp. *lycopersici* (*Fo*) race 2 isolate 4287 (FGSC 9935) was used throughout this study. For microconidia production, the strain was cultured in Yeast extract Peptone Dextrose (YPD) medium at 28 °C with orbital shaking (160 rpm) for 3–5 days until extensive sporulation was observed [62]. Microconidia were collected by filtration through a sterile nylon mesh (10 µm pore size) to remove mycelia, followed by centrifugation at 5,000 rpm for 10 min. The pellet was resuspended in sterile distilled water, and conidial concentration was determined using a Bürker counting chamber. Conidial suspensions were adjusted to the required density for each experimental application using serial dilutions in sterile distilled water, with final concentrations ranging from 1×10^4 to 1×10^6 conidia/mL depending on the specific assay requirements. Fresh conidial preparations were used immediately for all experiments or alternatively stored at − 80 °C in 30% glycerol until further use.

Growth inhibition assays

Growth inhibition assays were performed in 96-well microtiter plates using a spectrophotometric method. Fresh conidia of *F. oxysporum* were resuspended in Germination Medium (GM) [63]. Conidial suspensions (319×10^6 conidia/mL) were incubated with WMR-4 at concentrations ranging from 10 to 100 µM, or with nanofiber formulations (NF) at concentrations from 2.5 to 40 µM. Control wells contained only GM. Growth was monitored by measuring absorbance at 600 nm every 30 min for 14 h using a multiplate reader (Tecan Infinite 200 Pro F Nano$^+$; Tecan, Männedorf, Switzerland). All treatments were performed with at least three biological replicates, and experiments were conducted on at least two independent occasions. Results are presented as means ± standard deviation, with significance levels set at $p<0.05$ (*), $p<0.01$ (**), $p<0.001$ (***), and $p\leq0.0001$ (****).

Germ tube formation assays

Germ tube formation was monitored using an oCelloScope automated imaging system and UniExplorer software (version 11.1.0.8756) (BioSense Solutions ApS, Denmark). Fresh conidia of *F. oxysporum* (1.5×10^4 conidia per well) were resuspended in GM buffered to pH 7.0 and distributed into 96-well plates with test compounds at the same concentrations used in growth inhibition assays. Objects were scanned every 30 min for 14 h, with measurements initiated after 15 min of incubation to allow complete conidia settling. The oCelloScope then analyzed and normalized the corresponding changing fungal mass over time per well (n = 3 per tested condition) using a built-in microconidia algorithm which then generated the raw data for the growth curves through a segmentation and extraction of surface areas algorithm in order to quantify morphological changes. At least 500 individual conidia were tracked per well, with three biological replicates per treatment. Statistical analysis was performed using appropriate tests for comparison of germination rates between treatments, with data presented as means ± standard deviation.

Membrane interaction studies

Liposome preparation

Large unilamellar vesicles (LUVs) were prepared to mimic the *Fusarium oxysporum* membrane, made of POPC/POPE/PS/PI/Ergosterol (30:18:6:6:40, ratio in moles) [64]. Lipid films were prepared by mixing at the specific ratio phospholipids dissolved in chloroform. The organic solvent was removed under a nitrogen stream, and lipid film was lyophilized at overnight. Then, for multilamellar vescicles (MLVs), the lipid films were rehydrated in buffer/water for 1 h [65]. The lipid suspension was then subjected to six freeze–thaw cycles, followed by extrusion through polycarbonate membranes (pore size: 0.1 µm) for 10 times to obtain homogeneous LUVs. While, small unilamellar vesicles (SUVs) were obtained by sonication of MLVs for 40 min.

Peptide oligomerization in the fungal membrane

Peptide oligomerization was monitored by Thioflavin T (ThT) assay in the presence of LUVs. In particular, the lipid films were hydrated in a buffer containing 100 mM NaCl, 10 mM Tris–HCl, and 25 µM ThT at pH 7.4, for 1 h [61, 66]. Then, the suspension was treated as described above to obtain LUVs. LUVs were titrated with the peptide WMR-4 at the concentrations of 5, 10, 15, 20, 30, and 50 µM. ThT fluorescence was recorded before and after the addition of WMR-4 using a Varian Cary Eclipse fluorescence spectrophotometer. The emission spectrum was measured at 482 nm upon excitation at 450 nm. Peptide aggregation was expressed as the percentage increase in ThT fluorescence according to the following equation:

$$\frac{(Fi - F_0)}{(F_{max} - F_0)}x100$$

where F_i indicates the fluorescence after peptide addition, F_0 the initial fluorescence in the absence of peptide and F_{max} is the fluorescence maximum obtained immediately after peptide addition.

Lipid mixing assay

Fluorescence resonance energy transfer (FRET) assay was used to evaluate the fusogenic activity of WMR-4 in the presence of LUVs mimicking fungal membrane [67]. Two different set of liposomes were prepared to perform the lipid mixing assay. Specifically, we prepared unlabeled-LUVs made of POPC/POPE/PS/PI/Ergosterol (30:18:6:6:40) and labeled-LUVs containing also NBD as donor and Rho as acceptor probes. Vesicles labeled with 0.6 mol% of each fluorophore were mixed with unlabeled vesicles at a 1:4 ratio, yielding a final total lipid concentration of 0.1 mM [68]. The LUVs' fusion was measured by adding the peptide WMR-4 solutions at the concentrations of 2.5, 5, 10, 15, 20, 30, and 50 μM. At each addition, we recorded the emission of NBD at 530 nm following excitation at 465 nm. The fluorescence scale was calibrated by defining 0% as the residual donor fluorescence measured before the onset of membrane fusion, and 100% as the maximum fluorescence obtained upon complete lipid mixing, induced by the addition of Triton X-100 (0.05%, v/v) at the same total lipid concentration used in the assay.

The equation for calculating the percentage of fusion is as follows:

$$\frac{[F530/F590]peptide\ -[F530/F590]blank}{[F530/F590]triton\ -[F530/F590]blank}\ x\ 100$$

where F530 and F590 represent the intensity at 530 nm and 590 nm, respectively, which we calculated in the presence and absence of the peptide and triton. All experiments were repeated at least three times; results are presented as average values.

Calcein leakage assay

The calcein leakage assay was used to monitor the ability of WMR-4 to induce pore formation on the fungal membrane. Once prepared lipid film, it was hydrated with buffer 10 mM Tris, 150 mM NaCl (pH 7.4) and 60 mM calcein for 1 h under stirring [69]. The vesicles were extruded through polycarbonate membranes to obtain LUVs. To remove non-encapsulated calcein, free calcein was removed by gel filtration using a Sephadex G-25 column (1.5 × 10 cm; Pharmacia Biotech AB, Uppsala, Sweden) at rt. The leakage activity was evaluated by treating LUVs with WMR-4 at the concentrations of 2.5, 5, 10, 15, 20, 30, and 50 μM. Calcein fluorescence was recorded with excitation and emission wavelengths set at 485 nm and 535 nm, respectively. The leakage percentage was calculated by measuring the calcein release from liposomes and according to the formula:

$$\%Leakage = \frac{Fi - F0}{F - F0}\ x\ 100$$

where F0 is the initial fluorescence intensity prior to peptide addition, Ft is the fluorescence intensity after the peptide addition, F corresponds to the fluorescence following complete liposome disruption induced by the addition of Triton X-100 (0.1%, v/v).

WMR-4 insertion into the fungal membrane

The WMR-4 insertion into lipid bilayers was studied by performing the quenching of the tryptophan (Trp) residue with acrylamide, a water-soluble quencher that is not able to insert in the membrane [70]. The quenching assay was performed in the presence of LUVs mimicking *Fusarium oxysporum* membrane and buffer. The peptide WMR-4 at 20 μM in aqueous buffer was quenched by adding increasing concentrations of acrylamide from 0.02 M to 0.16 M [53]. In the presence of LUVs (final lipid concentration: 100 μM), WMR-4 was incubated at 20 μM and the acrylamide was added at the same concentrations. In both conditions, the Trp fluorescence spectrum was recorded for each acrylamide concentration exciting at 295 nm. The data were analyzed according to the Stern–Volmer equation to calculate the Stern–Volmer quenching constant that reflects the degree of tryptophan exposure to the aqueous environment and provides insight into peptide insertion into the lipid bilayer. The formula is $F0/F = 1 + K_{sv}\ [Q]$, where F0 and F represent the fluorescence intensities in the absence and presence of the quencher (Q), respectively.

In addition, the Trp insertion was further investigated using α-chymotrypsin assay and in the presence of Small Unilamellar Vesicles (SUVs). Firstly, once prepared the lipid film, it was hydrated with the buffer 100 mM Tris–HCl (pH 7.3) for 1 h, and then sonicated for 40 min to obtain SUVs. The α-chymotrypsin assay was performed both in buffer and SUVs, monitoring the Trp fluorescence emission after the proteolytic cut by the enzyme. Chymotrypsin has a strong affinity towards aromatic amino acids [71], cuts peptide bonds involving Trp residues, resulting in an increase in Trp fluorescence. In the buffer condition, the peptide was prepared at a concentration of 20 μM in 100 mM Tris–HCl (pH 7.3) and was incubated with 3 μM chymotrypsin. Fluorescence emission was monitored for 15 min using excitation and emission wavelengths of 295 and 355 nm, respectively. The same experiment was performed in SUVs (250 μM), where WMR-4 was incubated at 20 μM, and then the enzyme was added.

Cellophane penetration assay

The ability of *F. oxysporum* to penetrate plant-mimetic barriers was assessed using cellophane membrane assays adapted from previous studies [72]. Briefly, fungal penetration capacity was assessed using autoclaved colorless cellophane membranes (Manipulados Margok) placed on minimal medium (MM) containing 30 g/L sucrose, 0.5 g/L KCl, 0.5 g/L $MgSO_4{\cdot}7H_2O$, 1 g/L KH_2PO_4, and 2.1 g/L $NaNO_3$, pH 5.5. Test compounds or water (control) were applied topically by spreading 100 µL of each solution uniformly onto the cellophane surface using a sterile spatula, followed by air drying under sterile conditions for complete solvent evaporation. WMR-4 was tested at 80 µM final concentration and NF formulations at equivalent WMR-4 concentration. Control plates contained MM without antifungal compounds. Membrane centers were then inoculated with 4 µL of microconidial suspension containing 5×10^4 *F. oxysporum* conidia and incubated at 28 °C for 72 h under sterile conditions. Penetration assessment involved careful membrane removal followed by an additional 24-h incubation period to allow visualization of successfully penetrated fungal hyphae on the underlying agar surface. Colonies were imaged both before membrane removal (total mycelia) and after the additional incubation period (penetrated mycelia) with an Epson Perfection V850 Pro scanner using the Epson Scan Windows application Version 3.9.3.4 US with 24-bit colour and 300 dpi resolution (Epson Europe, Amsterdam, The Netherlands). Each experimental condition included a minimum of three replicate plates, and experiments were conducted at least twice to ensure reproducibility.

Quantitative analysis of fungal penetration was performed using ImageJ software to assess fungal biomass density through gray-level intensity measurements [73]. For each scanned image, the following standardized protocol was applied: images were first converted from RGB format to 8-bit grayscale and gray-level quantification was performed using the ImageJ line selection tool to measure colony intensity values across standardized regions of interest. For each colony, line measurements were taken across the fungal growth area both before membrane removal (surface growth) and after the additional 24-h incubation period (penetrated growth beneath the membrane). Background correction was applied by subtracting gray values from adjacent areas lacking mycelial growth. Mean gray values were calculated for each individual plate, treatment condition, and time point to generate representative quantitative data for statistical analysis.

The line tool measurements allowed for assessment of spatial distribution patterns of penetration zones, while mean values derived from multiple measurements across replicates provided quantitative measures of penetration abundance under each experimental condition. Data were exported in.csv format for subsequent statistical analysis, with penetration capacity expressed as mean gray values (arbitrary units, a.u.) ± standard deviation from biological replicates.

Statistical differences between treatment groups were evaluated using appropriate tests as specified in individual experiments, with significance levels set at $p<0.05$. All quantification procedures were performed in a standardized manner to ensure reproducibility and comparability across experimental conditions and time points.

Nanofiber formulation

WMR-4 was conjugated to the self-assembling peptide P2 to enable its delivery via a supramolecular nanofiber system. The nanofiber was prepared by co-assembling two structural peptides P1 and P2, with the peptide P3 carrying the cell-penetrating peptide gH625, and the peptide P2-a bearing WMR-4. The nanofibers used in the work are reported in Table 2.

Formulation	Peptide	Peptide ratio (in molar ratio)
NF-gH	P1 + P2 + P3	50:40:10
NF	P1 + P3 + P2-a	50:10:40

Nanofiber characterization by fluorescence-based assays

Firstly, we calculated the critical aggregation concentration (CAC) of P1, P2, P3, and P2-a in combination with each other at the specific ratios [61]. Each peptide was initially dissolved in HFIP at 200 µM and then combined at defined ratios to achieve final nanofiber concentrations of 0.8, 1, 3, 5, 7, 10, 15, 20, 30, 50, 100, 150, and 200 µM. The solvent HFIP was subsequently evaporated under a

Table 2 Characterization of designed peptide-based nanofibers

Nanofiber	Peptide composition	Peptide ratio	CAC (µM)	Zeta potential (mV)
–	P2-a	100	12.2 ± 0.1	+ 20.6 ± 5.2
NF-gH	P1 + P2 + P3	50:40:10	15.2 ± 0.9	+ 20.8 ± 1.6
NF	P1 + P3 + P2-a	50:10:40	7.2 ± 0.1	+ 33.2 ± 0.9

gentle nitrogen stream. The resulting films were rehydrated with 500 µL of water, sonicated for 15 min, and freeze-dried to promote self-assembly. For fluorescence measurements, each lyophilized sample was hydrated with 500 nM Nile Red in water and incubated for 1 h. The emission spectra were collected between 570 and 700 nm (slit width: 5 nm), with excitation set at 550 nm (slit width: 10 nm). The interaction of Nile Red with hydrophobic peptide aggregates is indicated by a characteristic blue-shift and an increase in fluorescence intensity, reflecting the dye's transition from aqueous environment into the hydrophobic core of the aggregates [74].

For the CAC determination, each maximum emission fluorescence corresponding to the wavelength (y) was plotted as a function of the peptide concentration using the following sigmoidal Boltzmann equation:

$$y = \frac{A1 - A2}{1 + e^{(x - x^0)/\Delta x)}} + A2$$

where A1 and A2 correspond to the upper and lower limits of the sigmoid, respectively. Instead, x_0 and Δx represent the inflection point and the steepness of the sigmoid, respectively.

The aggregation behavior of nanofibers containing the gH625 and WMR-4 peptide sequences was further investigated using ThT assay [61, 75]. Nanofibers P1 + P2 + P3 (50:40:10 in molar ratio) and P1 + P3 + P2a (50:10:40 in molar ratio) were prepared by mixing all peptides at the specific ratio, the organic solvent was removed under nitrogen stream, and they were lyophilized at overnight. Then, the film was hydrated with PBS 1X for 1 h, and then ThT was added at 25 µM. The fluorescence intensity of ThT was measured both in water and in both nanofibers.

Nanofiber characterization by dynamic light scattering

Dynamic light scattering (DLS) measurements to determine the zeta potential of nanofibers were made using Zetasizer Nano-ZS (Malvern Instruments, Worcestershire, UK). The nanofibers P1 + P2 + P2-a, P1 + P3 + P2-a, and P1 + P2 + P3 were prepared at 100 µM and the analysis was performed with He–Ne laser 4 mW operating at 633 nm at scattering angle fixed at 173° and at 25 °C.

Structural characterization of the final nanofiber

The secondary structure and conformational stability of the final nanofiber P1 + P3 + P2a was assessed using circular dichroism (CD) spectroscopy. Nanofiber was prepared at a final concentration of 50 µM, After lyophilization and rehydration for 1 h to allow nanofiber self-assembly, CD spectra were recorded in the 195–260 nm wavelength range using a Jasco J-810 spectropolarimeter equipped with a 1.0 cm pathlength quartz cuvette at room temperature. Each spectrum represents the average of three scans and was expressed as molar ellipticity.

To investigate nanofiber stability, CD analyses were performed under varying conditions: (i) serial dilution (40, 30, and 20 µM), (ii) different pH values (3,7, and 10) and (iii) increasing ionic strength by adjusting NaCl concentrations from 1 to 5 mM. In each case, nanofibers were initially assembled at 50 µM and subsequently exposed to the specific test condition.

Tomato fruit penetration assay

To evaluate invasive growth inhibition in plant tissue, tomato fruits (cv. Daniela) were washed under running tap water and surface-sterilized by immersion in 70% ethanol for 1 min, followed by air drying under sterile conditions. Test compounds were applied as 5 µL drops directly onto the fruit surface and allowed to dry completely under sterile conditions for complete solvent evaporation. Subsequently, 5 µL of microconidial suspension (1×10^7 conidia/mL) was inoculated onto the treated surface area. WMR-4 was tested at 80 µM final concentration, while NF formulations were applied at equivalent WMR-4 concentrations. Control fruits received solvent drops followed by conidial suspensions without antifungal compounds. Fruits were incubated at 28 °C under 100% humidity conditions in sealed chambers. Colonization assessment included monitoring tissue degradation and mycelial mat formation on the fruit surface up to 7 days post-inoculation. Each treatment included a minimum of three fruits, and experiments were performed at least twice with consistent results.

Apple fruit saprophytic growth assay

Saprophytic growth capacity of *F. oxysporum* was evaluated using apple fruit slices (variety Golden Delicious) as described by López-Berges and coworkers [76]. *F. oxysporum* cultures were grown in liquid potato dextrose broth (PDB) at 28 °C with orbital shaking at 170 rpm for 4 days to obtain fresh microconidia suspensions. Apple fruits were surface-sterilized with 100% ethanol, air-dried, sliced (0.8 cm thickness) and placed in sterile Petri dishes. Test compounds were applied as 5 µL drops onto the fruit surface and allowed to dry completely before spot inoculation with 5 µL of a conidial suspension (1×10^7 conidia/mL). WMR-4 was tested at 80 µM, and NF formulations were evaluated at equivalent concentrations. Control slices received solvent alone followed by conidial inoculation. Slices were incubated at 28 °C under 100% humidity conditions. After 4 days, invasion depth, colony expansion, and tissue maceration were evaluated macroscopically and documented photographically. Each treatment was performed with a minimum of three apple

slices per condition, and experiments were repeated at least twice with consistent results.

Structural analysis of NF and tomato after the treatment

Sample preparation

Tomato skin was cut into disk-shaped samples with a 7 mm diameter for Atomic Force Microscopy (AFM) and Scanning Electron Microscopy (SEM) analysis. The lyophilized nanofiber (NF) and the lyophilized WRM-4 peptide were hydrated in deionized water for 1 h at room temperature prior to treatment of the tomato skin samples. Sample A was prepared by applying 3 µL of a 200 µM aqueous solution of the NF (containing 80 µM of WMR-4) to the tomato skin surface, followed by drying at room temperature under a ventilated fume hood. Similarly, Sample B was treated with 3 µL of an 80 µM WRM-4 peptide solution. As a control, Sample C was treated with 3 µL of deionized water. For AFM analysis, Samples A, B, and C were imaged immediately after drying. Additionally, a 3 µL aliquot of a 50 µM of NF (containing 20 µM of WMR-4) was deposited onto a muscovite mica surface for imaging. Sample preparation for AFM on mica followed the procedure described previously [77]. Briefly, muscovite mica, approximately 1 cm^2 in size, was chosen due to its ability to cleave cleanly along the < 001 > crystallographic plane, yielding large atomically flat areas. Upon cleavage, the mica surface exposes highly mobile K^+ ions, which can be readily exchanged with divalent cations at the solid–liquid interface. This ion exchange leads to a positively overcharged mica surface, facilitating the adsorption of negatively charged molecules such as peptide fragments. The mica was freshly cleaved using adhesive tape immediately prior to sample deposition to ensure surface cleanliness. A 3 µL aliquot of the solution was directly cast onto the freshly cleaved mica and allowed to dry via evaporation at room temperature under a ventilated fume hood. For SEM analysis, the samples were further prepared by fixation to ensure they could withstand the low pressure within the SEM column without compromising the integrity of their biomorphological structures [78] and Microanalysis, Edited by Heide Schatten, Cambridge]. Then, tomato skin disks were fixed in 3% glutaraldehyde in 0.025 M sodium phosphate buffer (pH 6.8) for 30 min at room temperature and after at 4 °C for 16 h. They were then rinsed in the same buffer before dehydration through a graded ethanol series. Tomato samples were critical point dried using CO_2. Samples were deposited on SEM stubs and coated with a 10 nm thick layer of gold (Au) using thermal evaporation at a deposition rate of 0.1 Å/s, a technique that ensures uniform and orthomorphic metallic coatings suitable for electron microscopy analysis. The gold coating serves to increase the surface conductivity of the samples, thereby minimizing charging effects during imaging and improving overall image quality, especially for non-conductive or partially conductive materials, as well as biological samples.

Atomic force microscopy

A XE-100 Atomic Force Microscopy (AFM) (by Park Systems) was used for the 3D topography reconstruction of treated and untreated tomato slices and the fiber reconstruction on mica surface. Surface imaging was obtained in non-contact mode using Silicon/aluminum coated cantilevers (SSS-NCHR 10 M; Park Systems) 125 µm long with a resonance frequency of 204–397 kHz nominal force constant of 42 N/m and a typical tip radius 2 nm (< 5 nm max). The scan frequency was typically 0.5 Hz per line and the images have 2048 × 2048 pixels. When necessary, the AFM images were processed by the in-home software (XEP, by Park Systems) by flattening, in order to remove the background slope; the contrast and brightness have been adjusted. Moreover, the XEP software has been used to statistically determine the average roughness of treated and untreated tomato skins.

Scanning electron microscopy

The morphological characterization of the gold-coated samples was carried out using a Field Emission Scanning Electron Microscope (FESEM), specifically the Carl Zeiss Gemini 460, which offers high-resolution imaging capabilities thanks to its field emission gun and advanced electron optics. Imaging was performed using an accelerating voltage of 5 kV for Sample C and 10 kV for Sample A, with beam currents of 9 pA and 41 pA, respectively. These parameters were selected to optimize surface resolution while minimizing beam-induced damage and charging artifacts. Secondary Electron (SE) and INlens (IN) detectors were used to examine the topography. The SE detector is highly sensitive to surface topography, providing detailed visualization of nanoscale features and surface textures. The INlens detector collects backscattered electrons from the deeper layers of the sample, making it particularly sensitive to material composition.

Statistical analysis

All experiments were performed with appropriate biological replicates as specified in individual method sections, with each experiment repeated independently at least twice to ensure reproducibility. For experiments meeting parametric assumptions, one-way analysis of variance (ANOVA) was performed followed by Tukey's honestly significant difference (HSD) post-hoc test for multiple comparisons between treatment groups. For direct comparisons between two experimental conditions (such as penetration assays comparing control versus treatment),

Student's t-test was employed with Bonferroni correction applied for multiple comparisons to control family-wise error rates. Statistical significance was defined as $p < 0.05$ (*), $p < 0.01$ (**), $p < 0.001$ (***), and $p < 0.0001$ (****). All data are presented as means ± standard deviation (SD) unless otherwise specified. Statistical analyses were performed using GraphPad Prism software (version 9.0, GraphPad Software Inc., San Diego, CA).

Results and discussion

WMR-4: a stability-optimized myxinidin derivative

The peptide WMR-4 (NH_2-W**Aib**IRRILKYGKR***s******k***-$CONH_2$), a modified version of WMR with Gly^2 replaced by the unnatural amino acid 2-aminoisobutyric acid (Aib) and Ser^{13} and Lys^{14} substituted by their D-enantiomers, was successfully designed and developed to enhance its proteolytic stability and antimicrobial application [53]. The combined modifications resulted in a peptide variant with significantly enhanced proteolytic stability compared to the native WMR. Notably, after 5 h of incubation in human serum, approximately 70% of WMR-4 remained intact, whereas the native WMR peptide was completely degraded within the same timeframe. Moreover, these local modifications also promoted an enhancement of antimicrobial activity of WMR-4 in terms of biofilm inhibition and eradication against strong species such as *C. albicans, S. maltophilia, and A. xylosoxidans* [53] These promising results prompted us to evaluate WMR-4 against *F. oxysporum*, with a view toward its potential application in agricultural settings.

Antifungal efficacy and membrane-disruptive mechanism of WMR-4 against *Fusarium oxysporum*

The activity of WMR-4 against *F. oxysporum* was evaluated by monitoring both fungal growth and germ tube formation. WMR-4 demonstrated dose-dependent inhibitory effects on both parameters, indicating its potential as an effective antifungal agent. In particular, growth inhibition assays revealed that WMR-4 significantly

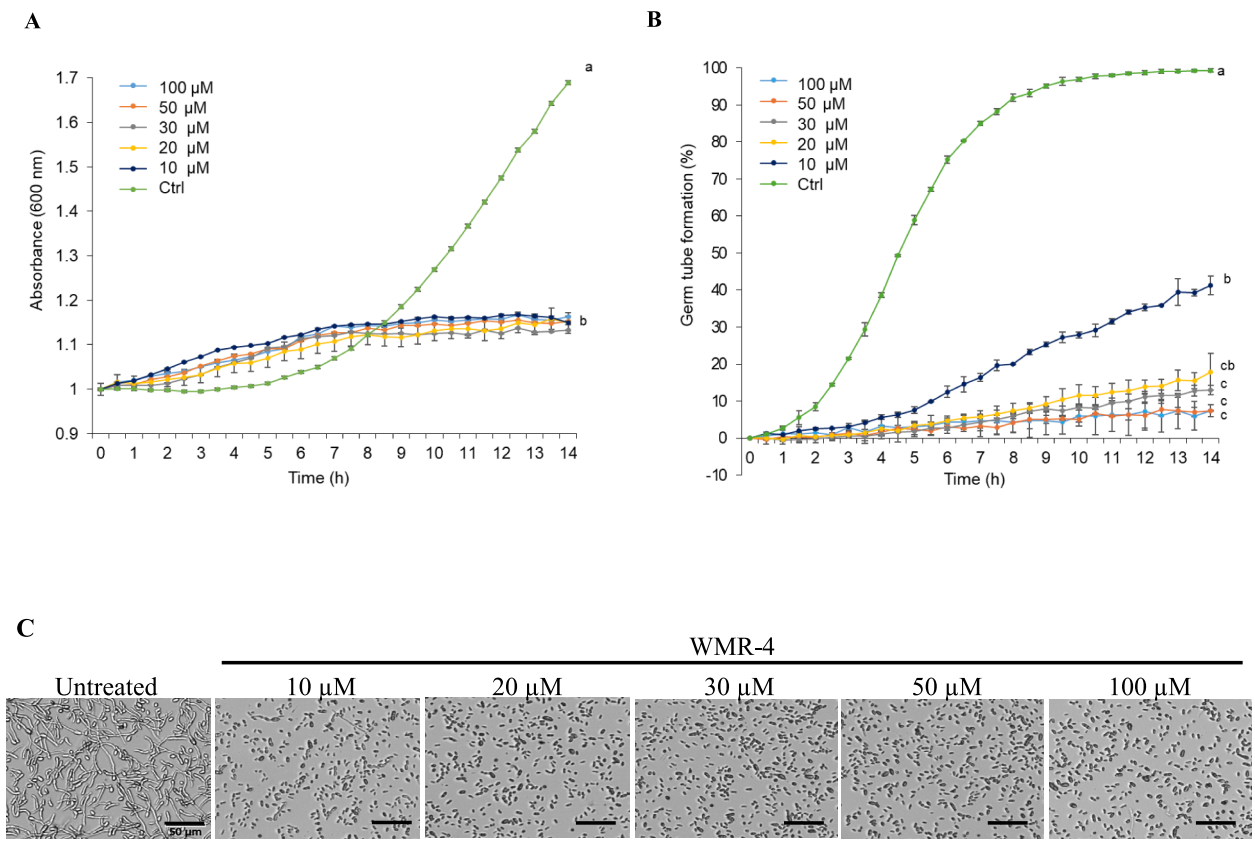

Fig. 1 WMR-4 inhibits *F. oxysporum* growth and germ tube formation. Panel **A**: Growth inhibition kinetics showing significant biomass reduction at all tested concentrations (10–100 µM) with plateau effects observed ≥ 30 µM. Panel **B**: Germ tube formation analysis revealing concentration-dependent inhibition with maximal reduction achieved at ≥ 30 µM. Panel **C**: Representative microscopy images demonstrating progressive inhibition of germination across the concentration range. Data represent means ± SD from biological replicates. Scale bar = 50 µm. Statistical significance determined by one-way ANOVA with Tukey's post-hoc analysis

reduced fungal biomass accumulation at all tested concentrations (10–100 μM) compared to untreated controls ($p < 0.0001$) (Fig. 1A). Even at the lowest concentration tested (10 μM), substantial antifungal activity was observed, demonstrating the peptide's potent inhibitory capacity. At concentrations of 30 μM and above, maximal growth suppression was achieved, with no statistically significant differences observed between these higher concentrations, indicating a plateau effect in the dose–response relationship throughout the 14-h observation period. Importantly, germ tube formation analysis demonstrated that WMR-4 effectively prevented conidial germination in a concentration-dependent manner (Fig. 1B). At 100 μM, WMR-4 reduced germ tube formation by approximately 62% compared to controls ($p < 0.0001$). Significant inhibition was also observed at lower concentrations, with 50 μM and 30 μM treatments showing reductions of 62% and 60%, respectively. Even at the lowest tested concentration (10 μM), WMR-4 still provided significant inhibition (47% reduction, $p < 0.05$). Statistical analysis using Tukey's multiple comparisons test revealed that all WMR-4 concentrations were significantly different from controls for both growth and germination parameters. Notably, concentrations of 30 μM and above showed no significant differences among each other, suggesting a plateau effect at higher concentrations.

To better understand its mechanism of action, we then carried out physicochemical studies using liposomes that mimic the membrane composition of *F. oxysporum*. These artificial membrane models allowed us to investigate, in a controlled environment, the potential interactions between the peptide and the fungal membrane, shedding light on the processes underlying its antimicrobial activity. For this aim, we prepared liposomes composed of POPC/POPE/PS/PI/Ergosterol (30:18:6:6:40, ratio in moles) that mimic the fungal membrane [64].

The membrane-disruptive activity of WMR-4 was assessed performing the lipid mixing and calcein release assays in LUVs. The lipid mixing assay was performed to evaluate the fusogenic activity of WMR-4 using labeled-LUVs with NBD and Rho mixed with unlabeled-LUVs. The fusogenic activity was calculated recording a decrease in donor fluorescence (NBD) and an increase in acceptor fluorescence (Rho) following the addition of increasing peptide concentrations ranging from 2.5 to 50 M.

As observed in Fig. 2A, WMR-4 showed a significant fusogenic activity causing a membrane fusion ~60% at the highest concentration of 20 M. In addition, the peptide WMR-4 also induced a marked increase in membrane permeability, with approximately 50% calcein leakage observed even at the lowest tested concentration of 10 M (Fig. 2B). This effect intensified with increasing peptide concentrations, reaching about 90% leakage at 30 μM. These results suggest that WMR-4 interacts with lipid bilayers in a concentration-dependent manner, promoting membrane destabilization and content release.

To further investigate the mechanism underlying this membrane activity, we assessed the peptide's ability to self-associate using Thioflavin T (ThT) fluorescence as a probe (Fig. 2C). A significant increase in ThT emission was observed in the presence of LUVs mimicking the fungal membrane, indicating that WMR-4 undergoes substantial oligomerization under these conditions. This aggregation may contribute to its membrane-disruptive effects.

To examine more closely the interaction and insertion of WMR-4 into lipid membranes, we performed Trp quenching experiments using acrylamide as a quencher (Fig. 2D). The intrinsic fluorescence of the Trp residue, located at the N-terminus of WMR-4, serves as a sensitive probe for peptide localization, as Trp emission increases in more hydrophobic environments. In this assay, acrylamide, being water-soluble and unable to penetrate lipid bilayers, selectively quenches Trp residues exposed to the aqueous environment. Thus, the deeper the Trp is inserted into the membrane, the lower its accessibility to acrylamide, resulting in reduced fluorescence quenching.

We monitored changes in Trp fluorescence upon exposure to increasing concentrations of acrylamide, both in aqueous solution [53] and in the presence of LUVs mimicking the fungal membrane. The degree of Trp accessibility in each condition was quantitatively assessed by calculating Stern–Volmer quenching constants (K_{sv}) through linear regression of the fluorescence data (Figs. 2E-2F). As already demonstrated previously, the Trp is fully accessible to quenching in water, where WMR-4 has a K_{sv} value of 15.4 ± 1.3 (Fig. 2F) [53]. In contrast, in the presence of LUVs, WMR-4 has a K_{sv} value of 2.1 ± 0.3, indicating clearly that the Trp residue is significantly more buried within the membrane environment. These findings support a strong interaction between WMR-4 and the lipid bilayer and suggest that the peptide adopts a membrane-inserted conformation in fungal-mimicking LUVs.

To further confirm the insertion of WMR-4 into the lipid membrane, we performed a proteolytic digestion assay using chymotrypsin after incubating the peptide with small unilamellar vesicles (SUVs) composed of POPC/POPE/PS/PI/Ergosterol (30:18:6:6:40, ratio in moles) (Figs. 2G-2H). Chymotrypsin selectively cleaves peptide bonds at hydrophobic residues; however, if the Trp residue is buried within the hydrophobic core of the membrane, it becomes inaccessible to enzymatic

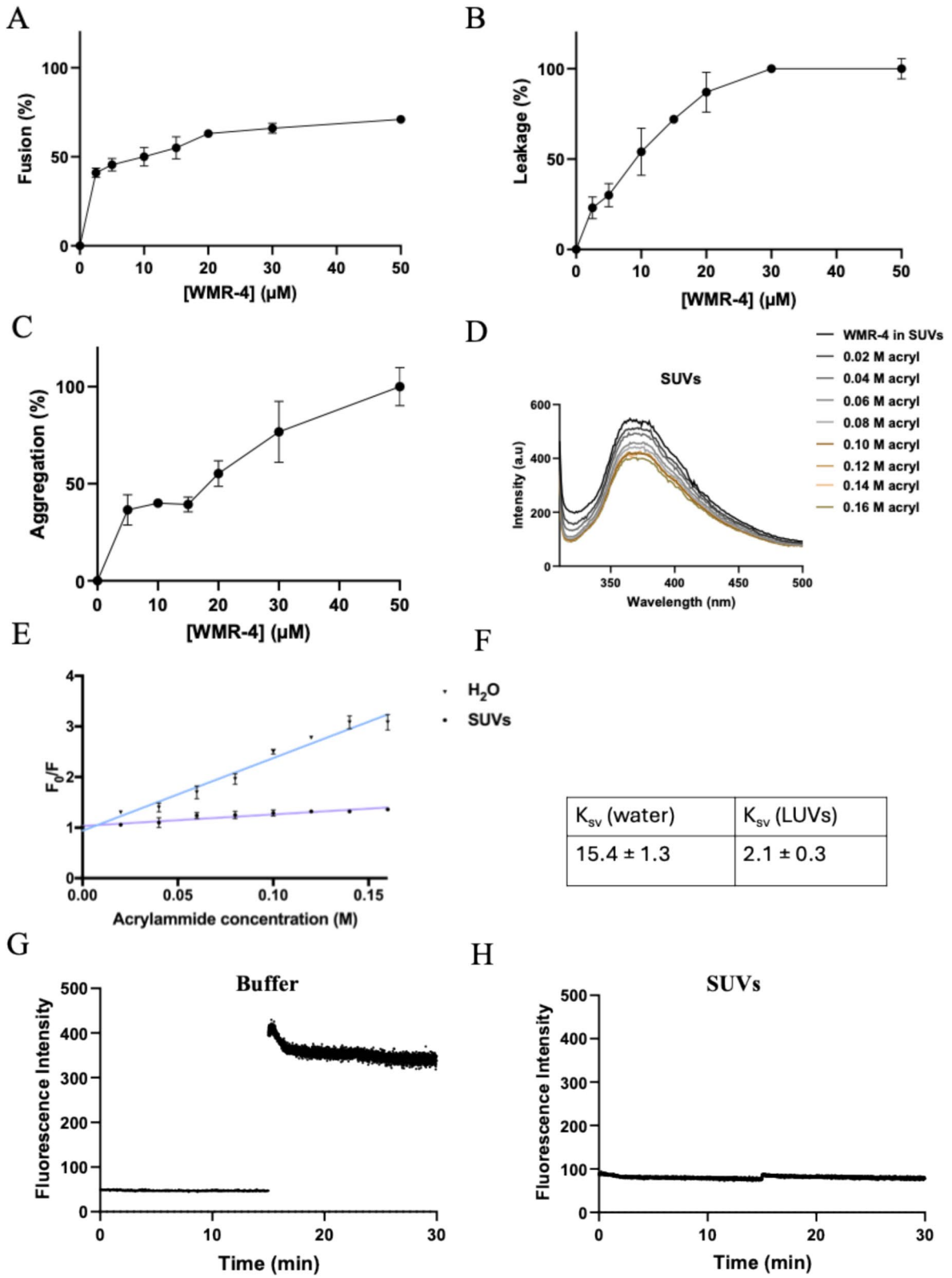

Fig. 2 WMR-4 membrane interaction with LUVs mimicking the *F. oxysporum* membrane. Panel **A**: Lipid mixing assay. Panel **B**: Leakage assay. Panel **C**: aggregation by ThT assay. Panels **D**–**F**: Fluorescence Trp spectra in SUVs after the quenching with acrylamide from 0.02 M to 0.16 M (**D**), and the data analyzed with the Stern–Volmer equation (**E** and **F**). Panels **G** and **H**: The fluorescence emission of WMR-4 with excitation set at 355 nm in buffer (**G**) and in LUVs (**H**) before and after the proteolytic cut by chymotrypsin

cleavage, resulting in minimal changes to its fluorescence emission.

We monitored changes in the quantum yield of Trp fluorescence before and after chymotrypsin treatment, both in buffer and in the presence of SUVs. As shown in Figs. 2G–2H, in buffer where Trp is fully exposed to the aqueous environment and the enzyme readily cleaves the peptide, leading to a significant increase in Trp fluorescence. In contrast, when the peptide is associated with SUVs, no appreciable increase in fluorescence was observed following enzyme addition. This indicates that Trp is shielded from enzymatic access, consistent with membrane insertion or deep association within the lipid bilayer. These results support and extend our previous findings, confirming that WMR-4 binds strongly to phospholipid membranes and is inserted into the lipid core or positioned at the bilayer interface, thereby protecting key residues from proteolytic cleavage.

Interestingly, in previous studies [53], we demonstrated that WMR-4 did not aggregate in LUVs mimicking Gram-negative bacterial membranes or *Candida albicans* membranes, despite clear evidence of membrane insertion in both systems. In those cases, Trp fluorescence data revealed partial accessibility to acrylamide quenching, suggesting that the peptide adopts a shallow or surface-associated orientation within the bilayer. Additionally, no significant liposome leakage was observed in the 5–50 μM concentration range, further supporting the absence of substantial membrane disruption. Based on these observations, we previously hypothesized that WMR-4 interacts with Gram-negative and *C. albicans* membranes via a carpet-like or alternative non-lytic mechanism.

In contrast, the present study reveals a distinct behavior of WMR-4 toward membranes mimicking the fungal membrane, specifically *F. oxysporum*. Here, the peptide not only inserts deeply into the lipid bilayer, as indicated by Trp quenching and proteolysis protection assays, but also undergoes aggregation and induces significant membrane leakage. These features are key indicators of a lytic mode of action and are consistent with the biological activity observed, thereby providing further insight into the mechanism underlying WMR-4's antifungal efficacy.

WMR-4 does not inhibit *F. oxysporum* penetration through cellulose-based membranes

To bridge the gap between in vitro efficacy and practical agricultural applications, we decided to evaluate WMR-4's ability to inhibit fungal penetration through cellulose barriers that mimic the structural challenges encountered during natural plant invasion. Importantly, despite WMR-4's efficient antifungal activity in liquid culture systems, cellophane membrane penetration assays revealed a critical limitation in its protective capacity against barrier invasion. Indeed, when applied topically at 80 μM concentration, well above the effective antimicrobial concentrations demonstrated in growth and germination inhibition assays, WMR-4 was unable to prevent *F. oxysporum* penetration through cellulose membranes.

Visual assessment of cellophane membrane penetration showed that fungal hyphae successfully traversed the membrane and established growth on the underlying agar surface in both control (water) and WMR-4-treated conditions (Fig. 3). The fungus retained its invasive capacity despite surface peptide treatment, with clear evidence of penetration visible after membrane removal (WMR-4 after). This finding highlighted the fundamental difference between antimicrobial efficacy in controlled culture environments and protective performance against natural invasion processes.

Nanoplatform design, synthesis and characterization

Based on the results obtained using cellophane system, where the peptide WMR-4 was unable to inhibit fungal penetration, it was fundamental to develop effective delivery strategies to overcome food-related barriers that limit peptide accessibility to invading pathogens. In this contest, we developed a delivery platform based on self-assembled peptides to transport WMR-4 and exert its antifungal activity against *F. oxysporum*. Self-assembled peptides have a strong ability to arrange in stable and structurally defined nanostructures such as nanofibers. In our design, the nanoplatform consists of two structural peptides P1 and P2 featuring a hexa-alanine sequence and a C19 lipid tail conjugated to the ε-amino group of a C-terminal lysine. This configuration forms the hydrophobic domain which is encapsulated within the fiber core. Both peptides, P1 and P2, have also a hydrophilic domain featured by two charged residues, positive (Arg-Lys) in P1 and negative (Asp) in P2. These residues were included to promote intermolecular hydrogen bonding and to enable additional associative interactions through their complementary charges.

In addition, the peptide P2 was also linked to the biological moieties that are designed to be on the nanofiber's surface. In our design, the surface was functionalized with the cell-penetrating peptide (namely gH625) able to cross membranes; and the WMR-4 as AMP able to inhibit the fungal growth (Fig. 4).

For the preparation of WMR-4 functionalized nanofibers, our starting point was the nanofiber made of P1:P2:P3 (50:40:10, molar ratio) called NF-gH, characterized previously by us for cancer applications [49]. The co-assembly of P1, P2, and P3 at this specific molar ratio has determined a value of critical aggregation concentration (CAC) of 15.2 ± 0.9 μM [49], indicating a good tendency

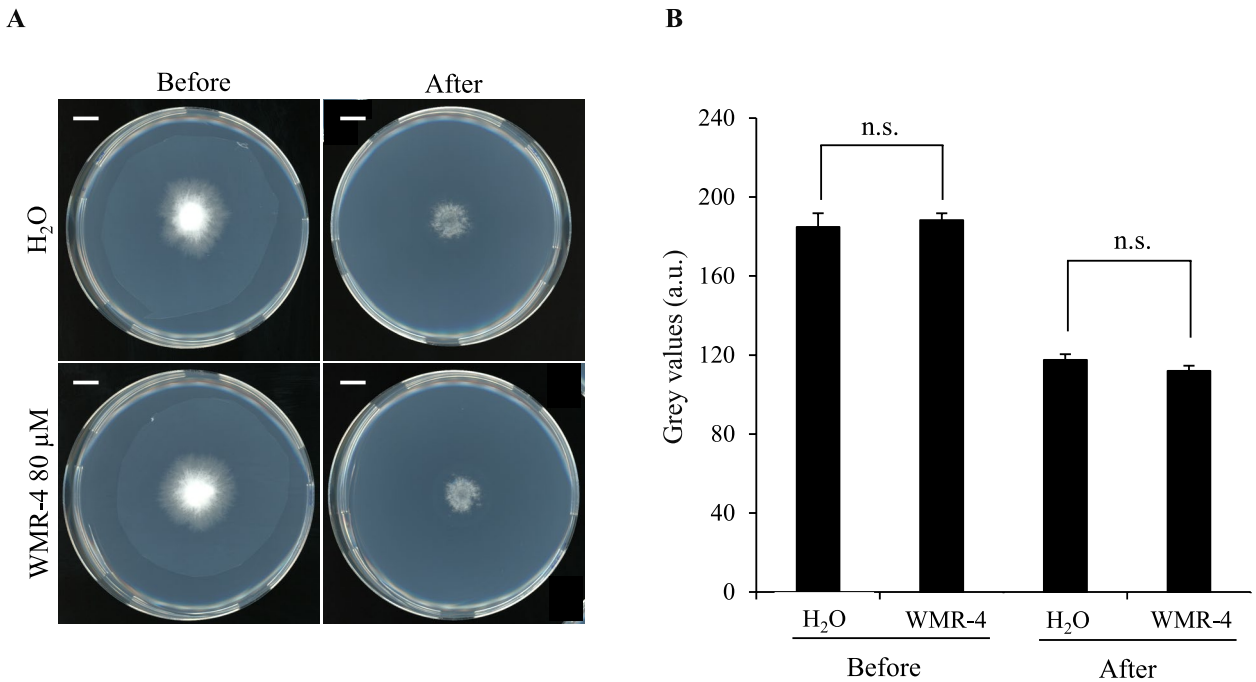

Fig. 3 WMR-4 does not inhibit *Fusarium oxysporum* membrane penetration. Panael **A**: Invasive growth of *F. oxysporum* on cellophane membranes placed on minimal medium (MM) with or without 80 µM WMR-4. Plates were imaged before and after cellophane removal to visualize penetration through the cellophane. Scale bar, 1 cm. Panael **B**: Quantitative gray-level analysis showing no significant reduction in surface and penetrated fungal biomass compared to controls

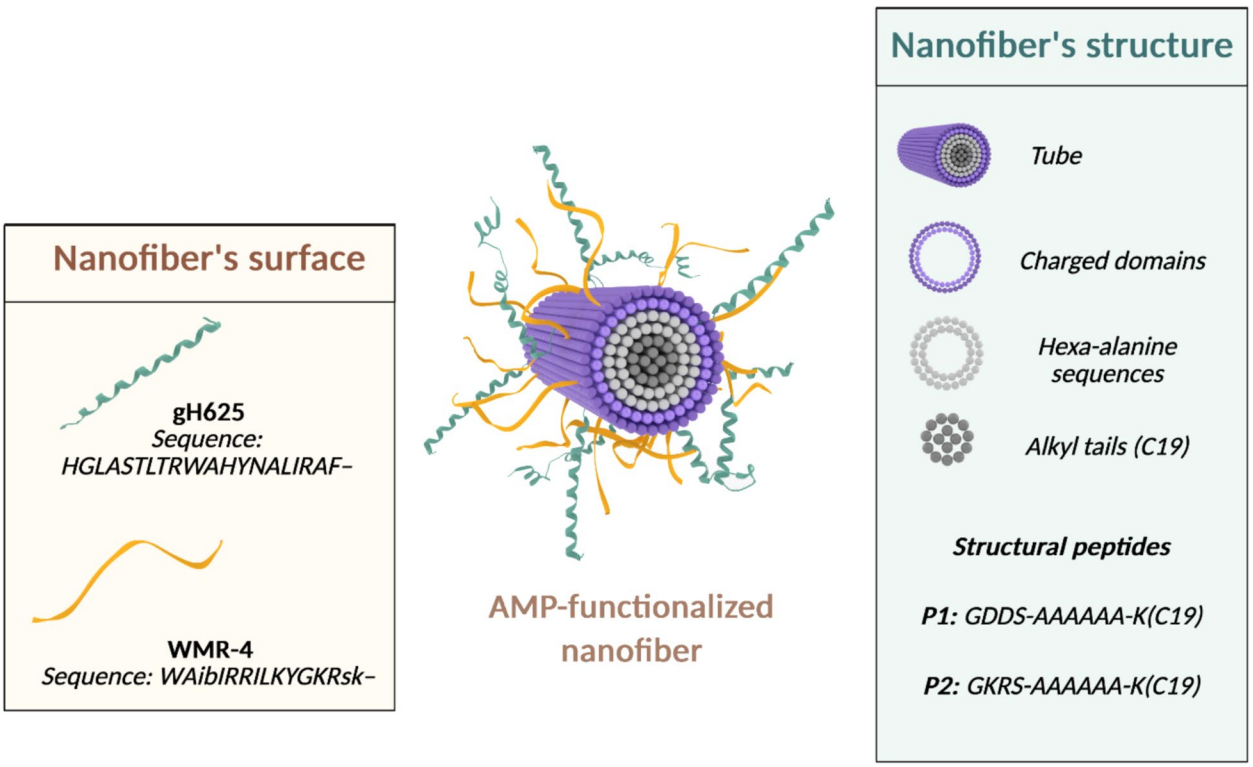

Fig. 4 Schematic representation of the nanofiber (NF)

to aggregate and form the nanofiber with a diameter of ca. 12 ± 2 nm and a length of ca. 150 ± 50 nm as observed by Transmission Electron Microscopy (TEM) image. For the WMR-4 functionalization on the surface of the nanofiber, the peptide WMR-4 was covalently linked to the peptide P2 obtaining P2-a that has a strong ability to aggregate alone with a CAC of 12.2 ± 0.1 μM (Table 2). When we co-assembled the peptide P2-a with P1 and P3 at the ratio 50:10:40 (P1:P3:P2-a) to form the nanofiber NF, where P2 was totally replaced by P2-a, we calculated

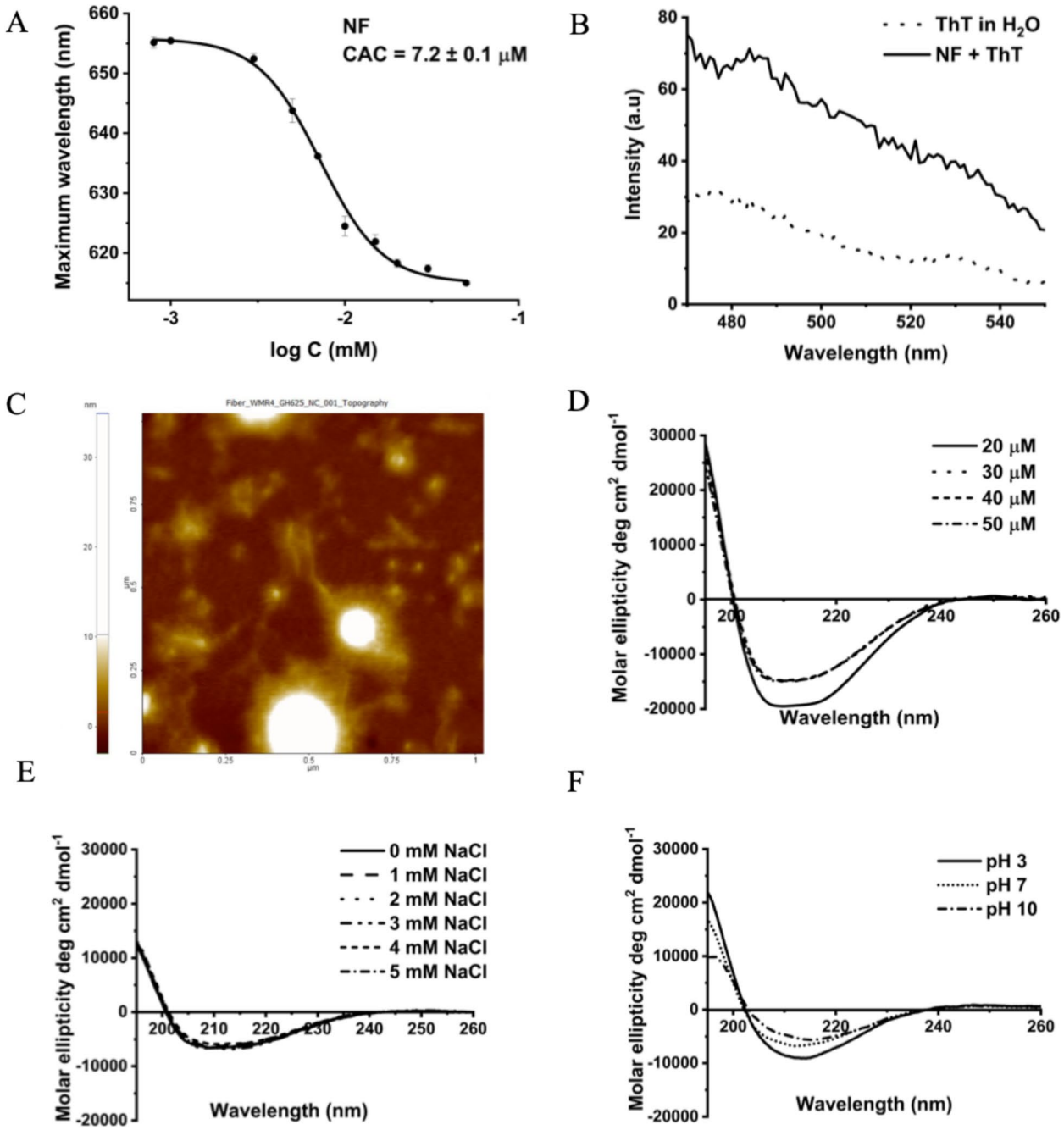

Fig. 5 WMR-4-functionalized nanofiber characterization. Panel **A**: Wavelength corresponding to the maximum fluorescence emission of Nile red was plotted as a function of the concentration nanofiber (NF) to determine the CAC value. Data represent the mean ± SD of three independent experiments. Panel **B**: ThT spectra recorded for NF and ThT alone in water. Panel **C**: AFM imaging of NFs deposited on mica superflat surface. Panels **D**–**F**: CD spectra of NF under dilution effect (**D**), ionic strength (**E**), and pH environments (**F**)

a CAC of 7.2 ± 0.1 μM (Fig. 5A). This ratio was chosen to keep the same WMR-4 concentration on the surface of the nanofiber that previously showed a good activity on the *Fusarium.*

The peptide assembly and nanofiber formation were also supported and investigated by Thioflavin (ThT) assay as highlighted in Fig. 5B. ThT is commonly used to monitor the formation of self-assembled nanostructures since its interaction within these structures hinders rotation between the benzene and benzothiazole rings resulting in enhanced fluorescence. After the NF hydration, ThT was added recording the enhancement of ThT emission approximately at 480 nm. The Fig. 5B showed an increase in ThT fluorescence supporting the peptide assembly and nanofiber formation. Moreover, the formation of nanofibers has been imaged by AFM on mica surface. The Fig. 5C showed the presence of nanofibers featured by a length between 200 and 300 nm and a diameter of about 25 nm.

In addition, the nanofiber NF was characterized in terms of charge surface by Dynamic Light Scattering (DLS, Table 2) and structural stability by Circular Dichroism (CD) spectroscopy. As reported in the Table 2, the analysis of the zeta potential revealed a positively charged surface for both NF-gH and NF, with NF exhibiting a higher value of + 33.2 ± 0.9 mV, likely due to the elevated concentration of WMR-4 on the surface, which is important for the interaction with negatively charged microorganism membranes. Moreover, the stability of the secondary structure of NF was investigated by Circular Dichroism (CD) spectroscopy. The nanofiber NF showed an a-helical conformation completely aggregated that has preserved its stability under dilution effect, ionic strength, and pH environments (Figs. 5D–F).

Nanofiber delivery systems demonstrate substrate-dependent antifungal efficacy and enhanced tissue protection

To address the limitations of WMR-4, we evaluated the antifungal performance of our supramolecular nanofiber delivery platform across multiple substrate models. NFs functionalized with WMR-4 displayed distinct activity patterns compared to the free peptide. Growth inhibition assays showed that NF formulations had minimal impact

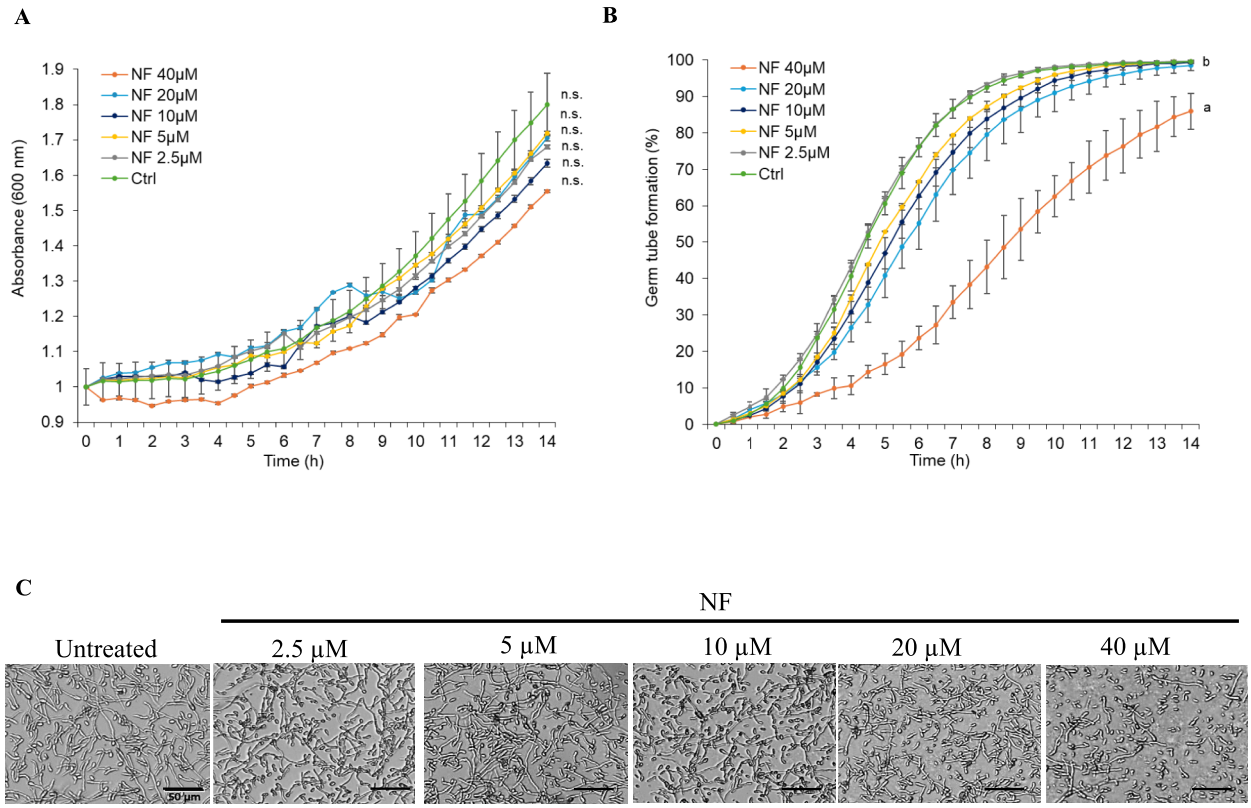

Fig. 6 NFs only inhibits *F. oxysporum* germ tube formation at high concentrations**.** Panel **A**: Growth kinetics demonstrating minimal impact on fungal biomass accumulation across tested NF concentrations (2.5–40 μM). Panel **B**: Germ tube formation analysis showing significant inhibition only at the highest concentration (40 μM). Panel **C**: Microscopy images confirming concentration-dependent effects on germination morphology. Scale bar = 50 μm. Data represent means ± SD from biological replicates with statistical analysis by one-way ANOVA

on overall fungal biomass accumulation, with no statistically significant differences observed between treated and control groups across all tested concentrations (2.5–40 μM) (Fig. 6A). However, germ tube formation assays revealed a more selective effect, with the highest concentration tested (40 μM) significantly reducing germ tube formation compared to controls, while lower concentrations (20, 10, 5, and 2.5 μM) showed no significant inhibitory effects on germination (Fig. 6B). This suggests that the nanofiber delivery system may require higher local concentrations to achieve comparable efficacy to free WMR-4, possibly due to controlled release kinetics or altered bioavailability.

However, when we tested NF (equivalent to 80 μM WMR-4 and 20 μM gH625) in cellophane membrane penetration assays we noticed that *F. oxysporum* growth was substantially reduced in the presence of the nanofiber compared to untreated controls (Fig. 7A). Nonetheless, fungal hyphae maintained their capacity to penetrate the membrane barrier and the overall amount of fungal biomass successfully traversing and establishing growth on the underlying agar surface was notably diminished (Fig. 7B), likely as a direct consequence of the reduced proliferative capacity observed with NF treatment. These results indicate that NF treatment effectively impairs fungal proliferative capacity on solid surfaces while penetrative mechanisms remain mostly unaffected. The contrasting performance profiles of free WMR-4 versus NF formulations reflect predictable differences in peptide distribution kinetics across assay systems. While free WMR-4 demonstrates superior liquid culture activity through direct fungal cell contact and optimal bioavailability, its application to solid surfaces results in radial diffusion away from the application point, creating concentration gradients that diminish local antifungal effectiveness over time. Conversely, the nanofiber delivery system maintains surface adherence and sustained peptide concentrations at the application site, trading reduced liquid culture mobility for enhanced barrier protection capability. This mechanistic divergence validates our delivery system design, where apparent NF liquid culture limitations represent an acceptable compromise for dramatically improved performance in agriculturally relevant barrier-based applications.

To determine whether WMR-4 conjugated to the delivery system presented enhanced antifungal efficacy in more biologically relevant contexts, we subsequently evaluated nanofiber performance using natural plant tissue substrates. However, evaluation on natural plant tissues revealed substantially different results that distinguished between saprophytic colonization and barrier penetration mechanisms. Apple fruit slice assays, which expose internal tissues devoid of protective epidermal barriers, were employed to assess saprophytic growth capacity under nutrient-rich conditions. After 4 days of incubation, control fruits showed extensive tissue

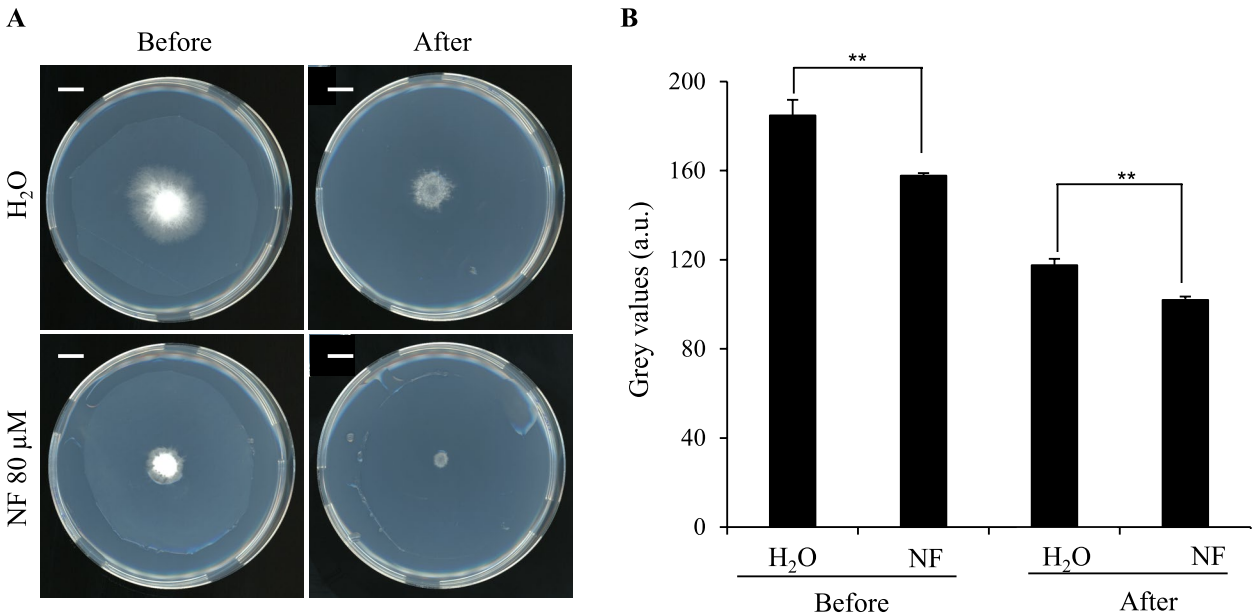

Fig. 7 NF partially inhibits *F. oxysporum* membrane penetration. Panel **A**: Cellophane membrane penetration assays showing reduced fungal growth (before) in NF-treated conditions while maintaining penetrative capacity (after). Scale bar, 1 cm. Panel **B**: Quantitative gray-level analysis demonstrating significant reduction in both surface and penetrated fungal biomass compared to controls. Statistical significance indicated by ** ($p < 0.01$)

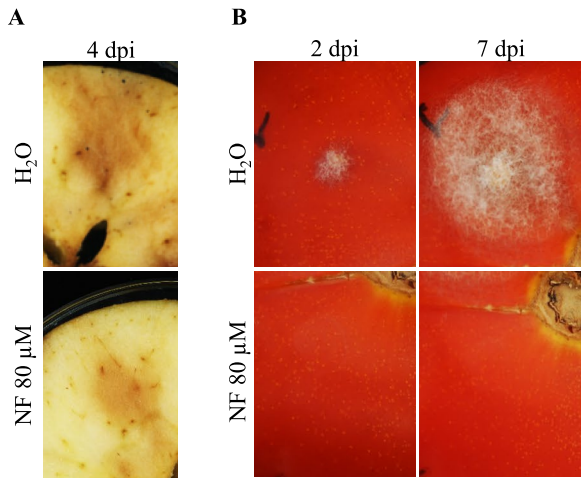

Fig. 8 NF demonstrates dual antifungal efficacy against saprophytic colonization and biological barrier penetration. Panel **A**: Saprophytic colonization assessment using apple slices showing enhanced tissue preservation and restricted fungal expansion in NF-treated samples compared to extensive maceration in controls. Panel **B**: Biological barrier penetration evaluation using intact tomato fruits demonstrating complete protection against mycelial mat formation and tissue degradation over 7 days post-inoculation

maceration, while NF-treated surfaces demonstrated substantially impaired saprophytic colonization with maintained tissue integrity and minimal fungal expansion (Fig. 8A). This indicated that NFs have significant antifungal efficacy against opportunistic tissue colonization in the absence of natural protective barriers.

In contrast, tomato fruit assays were designed to evaluate the ability of *F. oxysporum* to penetrate intact biological barriers, specifically the cutin-rich epidermal cell layers that constitute the primary defence against fungal invasion. These experiments simulated natural infection processes where pathogens must overcome sophisticated plant defence architectures to gain access to nutrient sources. While control fruits developed extensive mycelial mats and tissue degradation by 7 days post-inoculation, demonstrating successful breach of epidermal barriers, NF-treated surfaces showed no colonization and preserved tissue structure even after prolonged incubation periods (Fig. 8B). The enhanced protection observed in tomato assays suggested that NF provides superior efficacy against biological barrier penetration mechanisms compared to simple saprophytic growth inhibition.

The nanofiber coating on tomato was analyzed by SEM and AFM

The microscopy techniques, including SEM and AFM, were employed to investigate the formation of the nanofiber coating on tomato fruit that blocks fungal penetration and infection. The Fig. 9 (panel A–D) showed SEM images of a tomato skin disk treated with NF at 80 M, at various magnifications. The SEM images reveal the presence of long, intertwined NFs forming micrometer-scale clew ball-like structures (up to 15 µm in size), along with some residual material attributed to the sample fixation procedure (characterized separately in the control sample). The diameter of the NFs ranges between 10 and 30 nm. These formations indicate that the fixation process does not interfere with the binding of the NFs to the tomato skin surface, suggesting a strong interaction. Moreover, to confirm the presence of NF on tomato skin disk, we also recorded the SEM images of tomato skin disk treated with deionized water, used as a

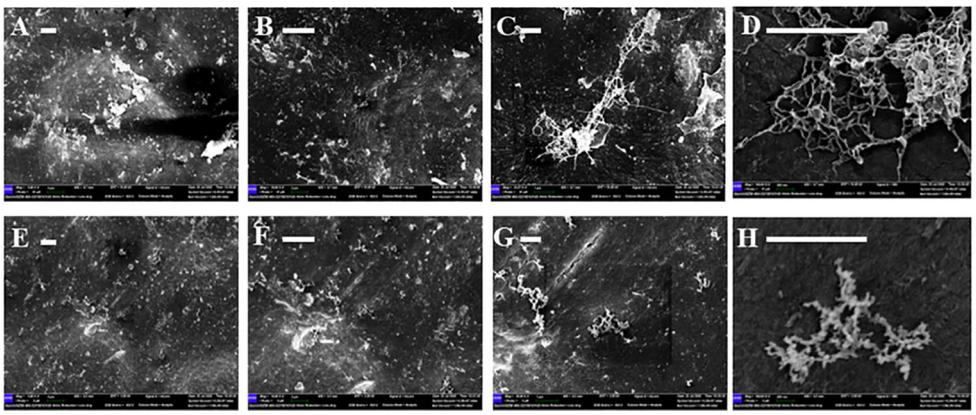

Fig. 9 SEM images of tomato skin disk treated NF at 80 µM and deionized water used as control. Panels **A**,**B**, and **C**: IN detector has been used in order to enhance the difference between the cellular material of the substrate and the organic compound of the NFs. Panel **D** underlines a clew ball formation where NFs are arranged on several layers (SE detector has been used, to enhance the topographic characteristics). Panels **E**–**H**: Images of tomato skin disk treated with water. Even if some cluster formations are present, due to residuals of fixing procedure, their aspect is quite different by NF for length and shape. In **A**, **B**, **E** and **F** scale bar is 4 m; In **C**, **D**, **G** and **H** scale bar is 1 µµ

control (Fig. 9E–H). As observed in Fig. 9, although some cluster-like formations are also visible on the untreated surface, likely due to residues from the fixation procedure, their morphology significantly differs from that of the NFs in terms of both shape and size. These clusters appear as rough aggregations of flake-like structures with diameters around 50 nm and lengths not exceeding 3 µm.

To investigate the effect of NFs on the surface morphology of tomato skin, we also conducted AFM analysis, which provides not only qualitative topographic imaging but also 3D surface reconstruction and quantitative roughness measurements (Fig. 10A–B). While the peak-to-valley roughness (R_{pv}) reflects the natural surface undulations caused by the cellular structure of the tomato, the average roughness (R_a) describes the finer-scale surface texture. In the control sample A (Fig. 10C), R_{pv} is approximately 80 nm and R_a is 7.4 nm, measured over a surface area of around 4 μm^2. For NFs (Fig. 10B), R_{pv} decreases to 52 nm and R_a to 5.3 nm over a similar area. These results suggest that the NFs not only coat the tomato surface, smoothing out its superficial roughness, but also tend to accumulate in the intercellular spaces, thereby reducing peak-to-valley height variations. This evidence supports our hypothesis regarding the potential mechanism by which the supramolecular delivery system interferes with fungal penetration and infection.

Conclusions

F. oxysporum represents a devastating soil-borne vascular pathogen that causes significant pre-harvest losses across over 100 plant species through its specialized *formae speciales*, each genetically adapted to specific hosts. Beyond its primary role in vascular wilt diseases, this versatile pathogen subsequently contributes to post-harvest food security challenges by accelerating tissue softening and promoting rapid maceration in fresh produce during storage and transport, thereby extending its economic impact throughout the entire production chain. This agricultural burden is compounded by the pathogen's emergence as a life-threatening opportunistic infection in immunocompromised humans, with mortality rates exceeding 80%. The dual agricultural-clinical threat is further exacerbated by rising antimicrobial resistance in fungi, creating an urgent need for innovative strategies that leverage advanced materials and nanotechnologies for next-generation control applications. In this study, we successfully demonstrated the translation of rational peptide design into practical antifungal solutions through supramolecular engineering approaches. Our systematic characterization of WMR-4 revealed potent antifungal activity against *F. oxysporum* mediated through a distinct lytic mechanism involving deep membrane insertion, peptide aggregation, and substantial membrane leakage. Biophysical studies employing liposome models and aggregation monitoring established that WMR-4 adopts a fundamentally different interaction mode with fungal membranes compared to bacterial and C. *albicans* membranes, highlighting the importance of pathogen-specific optimization in antimicrobial peptide development.

The critical discovery that free WMR-4 failed to prevent membrane penetration despite strong in vitro efficacy illuminated a fundamental translational barrier in peptide therapeutics. To overcome these barriers, we developed a supramolecular nanofiber platform functionalized with WMR-4 and the cell-penetrating peptide gH625. This delivery system, while limited in suppressing fungal biomass accumulation in vitro, inhibited germ tube formation and partially reduced fungal penetration through cellulose barriers. Notably, NFs possess significant antifungal efficacy under nutrient-rich conditions by preserving tissue integrity and reducing fungal expansion; thus, effectively limiting

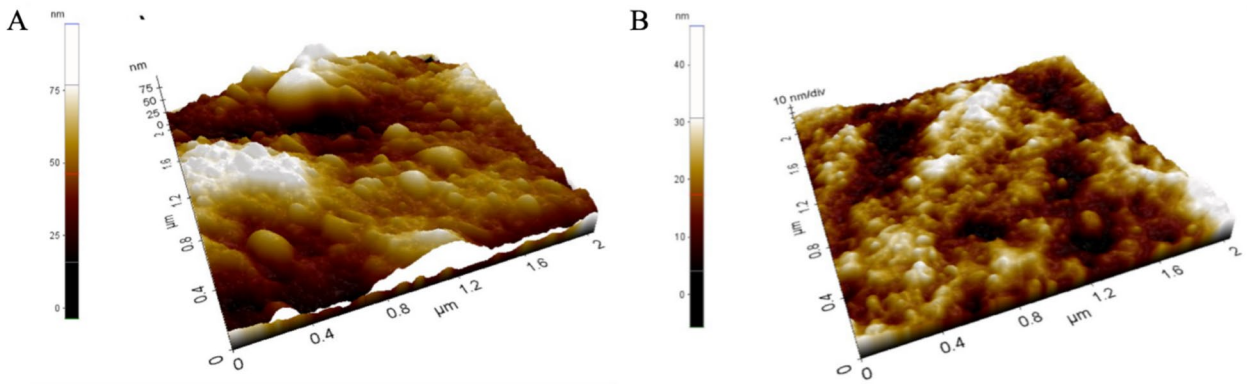

Fig. 10 AFM 3D reconstruction of tomato skin disk sample. Panel **A**: Tomato skin treated with deionized water as control. Panel **B**: Tomato skin treated with NF

opportunistic saprophytic colonization in apple tissues lacking epidermal barriers. Furthermore, NF treated tomato fruits remained resistant to fungal invasion, highlighting the potential of nanostructured delivery systems to provide barrier-specific protection. SEM and AFM analyses supported and confirmed that the NFs form stable, nanoscale coatings on plant surfaces, reducing surface roughness and integrating into epidermal layers, which may further contribute to their protective effects.

The modular design enables rapid adaptation to diverse phytopathogens through peptide substitution strategies. In particular, simple peptide modifications or substitutions can make the system effective against additional microbial strains creating a versatile technology for sustainable crop protection. Furthermore, our results establish a comprehensive translational framework demonstrating that effective progression from molecular design to practical implementation requires systematic addressing of biological complexity at multiple scales. By bridging advanced peptide chemistry with innovative nanotechnology platforms, this work provides a promising pathway toward next-generation crop protection strategies that simultaneously address antimicrobial resistance, environmental sustainability, and global food security challenges. The platform technology represents a significant advancement in applied antimicrobial research, offering both immediate agricultural benefits and a robust foundation for future biotechnology innovation.

Supplementary Information

The online version contains supplementary material available at https://doi.org/10.1186/s40538-025-00880-1.

Supplementary Material 1.

Acknowledgements
We gratefully thank Prof. Carla Langella and Dr. Giovanna Nichilò for the support in the design and science visualization of Fig. 4.

Author contributions
S. B. and O. E. A. and M. R. and L. E. I.: formal analysis, investigation, methodology. L. D. S. and D. T. and P. D and R.B.: data curation, investigation, writing—original draft. R. T. and C. C.: formal analysis, investigation. S. V. and A. F. and S. G.: data curation, formal analysis, investigation, writing—original draft, conceptualization, supervision, project administration, validation. All authors read and approved the final manuscript.

Funding
The work described in this paper was supported by the Agritech National Research Center and received funding from the European Union Next-Generation EU (PIANO NAZIONALE DI RIPRESA E RESILIENZA (PNRR)—MISSIONE 4 COMPONENTE 2, INVESTIMENTO 1.4–D.D. 1032 17/06/2022, CN00000022) to S.V., M.R., D.T and the Italian Ministry of Education, University and Research (PRIN 2022-TAKLPAT/2022SC83XK) to D.T. and Versatile lOaded Thera pAtch for Wound Skin Infections" (PRIN 2022/2022Y7HKJJ) nell'ambito del Fondo per il Programma Nazionale di Ricerca e Progetti di Rilevante Interesse Nazionale to A. F. and P.D. and "RNA Aptamer development for epigenetic control in neuropathic pain with specific delivery system: from theoretical to in vivo studies" nell'ambito del Fondo per il Programma Nazionale di Ricerca e Progetti di Rilevante Interesse Nazionale di Ricerca Bando PRIN 2022 PNRR to A:F.

Data availability
No datasets were generated or analysed during the current study.

Declarations

Ethics approval and consent to participate
Not applicable.

Consent for publication
Not applicable.

Competing interests
The authors declare no competing interests.

Author details
[1]Department of Pharmacy, School of Medicine, University of Naples Federico II, Via Domenico Montesano 49, 80131 Naples, Italy. [2]INTHERAPI Graduate School, Universite de Bourgogne, 21000 Dijon, France. [3]Department of Agricultural Sciences, University of Naples Federico II, Via Università 100, Portici, 80055 Portici, Italy. [4]Institute of Applied Sciences and Intelligent Systems, National Research Council, Naples, Italy. [5]Bioelectronics Task Force, University of Naples "Federico II", Naples, Italy. [6]Center for Studies On Bioinspired Agro-Environmental Technology, University of Naples Federico II, Via Università, 100, 80055 Portici, Italy. [7]Computational and Quantitative Biology Task Force, University of Naples Federico II, Naples, Italy. [8]Institute of Genetics and Biophysics Adriano Buzzati-Traverso (IGB-ABT) National Research Council, Naples, Italy. [9]Institute of Polymers, Composites and Biomaterials (IPCB) National Research Council, 80078 Pozzuoli, Italy.

Received: 23 August 2025 Accepted: 16 October 2025
Published online: 13 November 2025

References

1. Lee Y, Robbins N, Cowen LE. Molecular mechanisms governing antifungal drug resistance. NPJ Antimicrob Resist. 2023;1:5. https://doi.org/10.1038/s44259-023-00007-2.
2. Fisher MC, Alastruey-Izquierdo A, Berman J, Bicanic T, Bignell EM, Bowyer P, et al. Tackling the emerging threat of antifungal resistance to human health. Nat Rev Microbiol. 2022;20:557–71. https://doi.org/10.1038/s41579-022-00720-1.
3. Fisher MC, Henk DA, Briggs CJ, Brownstein JS, Madoff LC, McCraw SL, et al. Emerging fungal threats to animal, plant and ecosystem health. Nature. 2012;484:186–94. https://doi.org/10.1038/nature10947.
4. Ascioglu S, Rex JH, de Pauw B, Bennett JE, Bille J, Crokaert F, et al. Invasive fungal infections cooperative group of the European organization for research and treatment of cancer; Mycoses Study group of the national institute of allergy and infectious diseases, defining opportunistic invasive fungal infections in immunocompromised patients. Clin Infect Dis. 2002;34:7–14.
5. Almeida F, Rodrigues ML, Coelho C. The still underestimated problem of fungal diseases worldwide. Front Microbiol. 2019;10:214. https://doi.org/10.3389/fmicb.2019.00214.
6. Casadevall A. Climate change brings the specter of new infectious diseases. J Clin Invest. 2020;130:553–5. https://doi.org/10.1172/JCI135003.
7. Savary S, Willocquet L, Pethybridge SJ, Esker P, McRoberts N, Nelson A. The global burden of pathogens and pests on major food crops. Nat Ecol Evol. 2019;3:430–9. https://doi.org/10.1038/s41559-018-0793-y.
8. Brown GD, Denning DW, Gow NA, Levitz SM, Netea MG, White TC. Hidden killers: human fungal infections. Sci Transl Med. 2012;4:165rv13. https://doi.org/10.1126/scitranslmed.3004404.
9. Khaskheli MA, Nizamani MM, Tarafder E, Das D, Nosheen S, Muhae-Ud-Din G, et al. Sustainable management of major fungal phytopathogens in

Sorghum (*Sorghum bicolor L.)* for food security: a comprehensive review. J Fungi. 2025;11:207. https://doi.org/10.3390/jof11030207.
10. Steinberg G, Gurr SJ. Fungi, fungicide discovery and global food security. Fungal Genet Biol. 2020;144:103476.
11. Nicoletti R, Bellavita R, Falanga A. The outstanding chemodiversity of marine-derived talaromyces. Biomolecules. 2023;13:1021. https://doi.org/10.1016/j.fgb.2020.103476.
12. Martínez-Soto D, Yu H, Allen KS, Ma L-J. Differential colonization of the plant vasculature between endophytic versus pathogenic *Fusarium oxysporum* strains. Mol Plant Microbe Interact. 2023;36(1):4–13. https://doi.org/10.1094/MPMI-08-22-0166-SC.
13. Pietro AD, Madrid MP, Caracuel Z, Delgado-Jarana J, Roncero MI. *Fusarium oxysporum*: exploring the molecular arsenal of a vascular wilt fungus. Mol Plant Pathol. 2003;4:315–25. https://doi.org/10.1046/j.1364-3703.2003.00180.x.
14. Gordon TR. *Fusarium oxysporum* and the fusarium wilt syndrome. Annu Rev Phytopathol. 2017;55:23–39. https://doi.org/10.1146/annurev-phyto-080615-095919.
15. Srinivas C, Nirmala Devi D, Narasimha Murthy K, Mohan CD, Lakshmeesha TR, Singh B, et al. *Fusarium oxysporum f. sp. lycopersici* causal agent of vascular wilt disease of tomato: biology to diversity—a review. Saudi J Biol Sci. 2019;26:1315–24. https://doi.org/10.1016/j.sjbs.2019.06.002.
16. Ekwomadu TI, Mwanza M. Fusarium fungi pathogens, identification, adverse effects, disease management, and global food security: a review of the latest research. Agriculture. 2023;13:1810. https://doi.org/10.3390/agriculture13091810.
17. Agrios G. Plant pathology. 5th ed. Amsterdam: Elsevier Academic Press; 2005.
18. Dean R, Van Kan JA, Pretorius ZA, Hammond-Kosack KE, Di Pietro A, Spanu PD, et al. The top 10 fungal pathogens in molecular plant pathology. Mol Plant Pathol. 2012;13:414–30. https://doi.org/10.1111/j.1364-3703.2011.00783.x.
19. Vitale S, Turrà D. NO: from plant immunity to fungal virulence factor. Trends Plant Sci. 2025;30:699–701. https://doi.org/10.1016/j.tplants.2025.03.021.
20. Michielse CB, Rep M. Pathogen profile update: *Fusarium oxysporum*. Mol Plant Pathol. 2009;10:311–24. https://doi.org/10.1111/j.1364-3703.2009.00538.x.
21. Balasubramaniam J, Goh KS, Sani SF, Alam MW, Ismail NA, Gleason ML, et al. *Fusarium falciforme* and *F. oxysporum* causing postharvest fruit rot of watermelon (*Citrullus lanatus*) in Malaysia: a first report. Crop Prot. 2023;163:106115. https://doi.org/10.1016/j.cropro.2022.106115.
22. Mondani L, Chiusa G, Pietri A, Battilani P. Monitoring the incidence of dry rot caused by *Fusarium proliferatum* in garlic at harvest and during storage. Postharvest Biol Technol. 2021;173:111407. https://doi.org/10.1016/j.postharvbio.2020.111407.
23. Safari ZS, Ding P, Nakasha JJ, Yusoff SF. Controlling *Fusarium oxysporum* Tomato Fruit Rot under Tropical Condition Using Both Chitosan and Vanillin. Coatings. 2021;11:367. https://doi.org/10.3390/coatings11030367.
24. Zakaria L. *Fusarium* species associated with diseases of major tropical fruit crops. Horticulturae. 2023;9:322. https://doi.org/10.3390/horticulturae9030322.
25. Nucci M, Anaissie E. Fusarium infections in immunocompromised patients. Clin Microbiol Rev. 2007;20:695–704. https://doi.org/10.1128/cmr.00014-07.
26. Xu D, Wang K, Li T, Wang J, Wang S, Kong F, et al. In vitro activity of seven antifungal agents against *Fusarium oxysporum* and expression of related regulatory genes. PLoS ONE. 2025;20(4):e0322206. https://doi.org/10.1371/journal.pone.0322206.
27. Zheng Z, Liu H, Shi Y, Liu Z, Teng H, Deng S, et al. Comparative transcriptome analysis reveals the resistance regulation mechanism and fungicidal activity of the fungicide phenamacril in *Fusarium oxysporum*. Sci Rep. 2022;12(1):11081. https://doi.org/10.1038/s41598-022-15188-5.
28. Hudson O, Waliullah S, Ji P, Ali ME. Molecular characterization of laboratory mutants of *Fusarium oxysporum* f. sp. ***niveum*** resistant to prothioconazole, a demethylation inhibitor (DMI) fungicide. J Fungi. 2021;7(9):704. https://doi.org/10.3390/jof7090704.
29. Wightwick AM, Salzman SA, Reichman SM, Allinson G, Menzies NW. Effects of copper fungicide residues on the microbial function of vineyard soils. Environ Sci Pollut Res. 2013;20(3):1574–85. https://doi.org/10.1007/s11356-012-1114-7.
30. Varga K, Fehér J, Trugly B, Drexler D, Leiber F, Verrastro V, et al. The state of play of copper, mineral oil, external nutrient input, anthelmintics, antibiotics and vitamin usage and available reduction strategies in organic farming across Europe. Sustainability. 2022;14(6):3182. https://doi.org/10.3390/su14063182.
31. Gómez-Tenorio MA, Zanón MJ, de Cara M, Lupión B, Tello JC. Efficacy of dimethyl disulfide (DMDS) against *Meloidogyne* sp. and three formae speciales of *Fusarium oxysporum* under controlled conditions. Crop Prot. 2015;78:263–9. https://doi.org/10.1016/j.cropro.2015.09.013.
32. Marzano M, Gallo A, Altomare C. Improvement of biocontrol efficacy of *Trichoderma harzianum* vs. *Fusarium oxysporum* f. sp. *lycopersici* through UV-induced tolerance to fusaric acid. Biol Control. 2013;67(3):397–408. https://doi.org/10.1016/j.biocontrol.2013.09.008.
33. Bandara AY, Kang S. Trichoderma application methods differentially affect the tomato growth, rhizomicrobiome, and rhizosphere soil suppressiveness against *Fusarium oxysporum*. Front Microbiol. 2024;15:1366690. https://doi.org/10.3389/fmicb.2024.1366690.
34. O'Donnell K, Sutton DA, Rinaldi MG, Magnon KC, Cox PA, Revankar SG, et al. Genetic diversity of human pathogenic members of the *Fusarium oxysporum* complex inferred from multilocus DNA sequence data and amplified fragment length polymorphism analyses: evidence for the recent dispersion of a geographically widespread clonal lineage and nosocomial origin. J Clin Microbiol. 2004;42(11):5109–20. https://doi.org/10.1128/jcm.42.11.5109-5120.2004.
35. Zhang Y, Yang H, Turra D, Zhou S, Ayhan DH, Delulio GA, et al. The genome of opportunistic fungal pathogen *Fusarium oxysporum* carries a unique set of lineage-specific chromosomes. Commun Biol. 2020;3:50. https://doi.org/10.1038/s42003-020-0770-2.
36. Hawkins NJ, Cools HJ, Sierotzki H, Shaw MW, Knogge W, Kelly SL, et al. Paralog re-emergence: a novel, historically contingent mechanism in the evolution of antimicrobial resistance. Mol Biol Evol. 2014;31:1793–802. https://doi.org/10.1093/molbev/msu134.
37. Perlin DS, Rautemaa-Richardson R, Alastruey-Izquierdo A. The global problem of antifungal resistance: prevalence, mechanisms, and management. Lancet Infect Dis. 2017;17:e383–92.
38. Benish M, Elitzur S, Arad-Cohen N, Barg AA, Ben-Harosh M, Bielorai B, et al. Invasive fusariosis in pediatric hematology/oncology and stem cell transplant patients: a report from the Israeli Society of Pediatric Hematology-Oncology. J Fungi. 2022;8:387. https://doi.org/10.3390/jof8040387.
39. Zhou W, Li M, Achal V. A comprehensive review on environmental and human health impacts of chemical pesticide usage. Emerg Contam. 2025;11:100410. https://doi.org/10.1016/j.emcon.2024.100410.
40. Wu PH, Chang HX, Shen YM. Effects of synthetic and environmentally friendly fungicides on powdery mildew management and the phyllosphere microbiome of cucumber. PLoS ONE. 2023;18:e0282809. https://doi.org/10.1371/journal.pone.0282809.
41. Aunpad R, Thitirungreangchai T. Advancing antimicrobial peptides: overcoming challenges in the era of bacterial resistance. Biochimie. 2025;S0300–9084:00160–9. https://doi.org/10.1016/j.biochi.2025.07.019.
42. Rollins-Smith LA. The importance of antimicrobial peptides (AMPs) in amphibian skin defense. Dev Comp Immunol. 2023;142:104657. https://doi.org/10.1016/j.dci.2023.104657.
43. Zasloff M. Antimicrobial peptides of multicellular organisms. Nature. 2002;415:389–95. https://doi.org/10.1038/415389a.
44. Mahlapuu M, Håkansson J, Ringstad L, Björn C. Antimicrobial peptides: an emerging category of therapeutic agents. Front Cell Infect Microbiol. 2016;6:194. https://doi.org/10.3389/fcimb.2016.00194.
45. Brogden KA. Antimicrobial peptides: pore formers or metabolic inhibitors in bacteria? Nat Rev Microbiol. 2005;3:238–50. https://doi.org/10.1038/nrmicro1098.
46. Mookherjee N, Anderson MA, Haagsman HP, Davidson DJ. Antimicrobial host defence peptides: functions and clinical potential. Nat Rev Drug Discov. 2020;19:311–32. https://doi.org/10.1038/s41573-019-0058-8.
47. Yejiao S, Gan L, Borui Z, Zhinan L, Sumeng C, Zhe W, et al. Systematic all-hydrocarbon stapling analysis for cecropin a generates a potent and stable antimicrobial peptide. J Med Chem. 2025;68(6):6372–85. https://doi.org/10.1021/acs.jmedchem.4c02852.
48. Zhang Y, Zheng M, Wang Z, Liu Z, Chen S, Li X, et al. Discovery of novel antibacterial agent for the infected wound treatment: all-hydrocarbon stapling optimization of LL-37. Theranostics. 2024;14(3):1181–94. https://doi.org/10.7150/thno.87916.

49. Mengjun Z, Huixuan C, Xiang L, Si C, Yejiao S, Honggang H. Discovery of a novel antifungal agent: all-hydrocarbon stapling modification of peptide Aurein1. J Peptide Sci. 2023. https://doi.org/10.1002/psc.3533.
50. Khalifa HO, Oreiby A, Abdelhamid MAA, Ki MR, Pack SP. Biomimetic antifungal materials: countering the challenge of multidrug-resistant fungi. Biomimetics. 2024;9:425. https://doi.org/10.3390/biomimetics9070425.
51. Ntow-Boahene W, Cook D, Good L. Antifungal polymeric materials and nanocomposites. Front Bioeng Biotechnol. 2021;9:780328. https://doi.org/10.3389/fbioe.2021.780328.
52. Shi Y, Wareham DW, Phee LM, Azevedo HS. Self-assembled peptide nanostructures for antibacterial applications. In: Guler MO, editor. Peptide-based biomaterials. London: The Royal Society of Chemistry; 2020.
53. Cantisani M, Finamore E, Mignogna E, Falanga A, Nicoletti GF, Pedone C, et al. Structural insights into and activity analysis of the antimicrobial peptide myxinidin. Antimicrob Agents Chemother. 2014;58(9):5280–90. https://doi.org/10.1128/AAC.02395-14.
54. Bellavita R, Maione A, Braccia S, Sinoca M, Galdiero S, Galdiero E, et al. Myxinidin-derived peptide against biofilms caused by cystic fibrosis emerging pathogens. Int J Mol Sci. 2023;24:3092. https://doi.org/10.3390/ijms24043092.
55. Lombardi L, Shi Y, Falanga A, Galdiero E, de Alteriis E, Franci G, et al. Enhancing the potency of antimicrobial peptides through molecular engineering and self-assembly. Biomacromol. 2019;20:1362–74. https://doi.org/10.1021/acs.biomac.8b01740.
56. Liu H, Song Z, Zhang Y, Wu B, Chen D, Zhou Z, et al. De novo design of self-assembling peptides with antimicrobial activity guided by deep learning. Nat Mater. 2025;24:1295–306. https://doi.org/10.1038/s41563-025-02164-3.
57. Xu J, Liu T, Li Z, Liu R, Liu H, Lu J, et al. Amino acids and related polymers-mediated versatile noble metal nanomaterials: engineered design, antibacterial mechanisms and food preservation. Food Chem: X. 2025;29:102822. https://doi.org/10.1016/j.fochx.2025.102822.
58. Bellavita R, Braccia S, Falanga A, Galdiero S. An overview of supramolecular platforms boosting drug delivery. Bioinorg Chem Appl. 2023;2023:8608428. https://doi.org/10.1155/2023/8608428.
59. Li Y, Vrana NE, Letellier B, Lavalle P, Guilbaud-Chéreau C. The use of supramolecular systems in biomedical applications for antimicrobial properties, biocompatibility, and drug delivery. Biomed Mater. 2024;19:042005. https://doi.org/10.1088/1748-605X/ad49f4.
60. Galdiero S, Russo L, Falanga A, Cantisani M, Vitiello M, Fattorusso R, et al. Structure and orientation of the gH625-644 membrane interacting region of herpes simplex virus type 1 in a membrane mimetic system. Biochemistry. 2012;51:3121–8. https://doi.org/10.1021/bi201589m.
61. Maione A, de Alteriis E, Carraturo F, Galdiero S, Falanga A, Guida M, et al. The membranotropic peptide gH625 to combat mixed *Candida albicans/Klebsiella pneumoniae* biofilm: correlation between in vitro anti-biofilm activity and in vivo antimicrobial protection. J Fungi (Basel). 2021;7:26. https://doi.org/10.3390/jof7010026.
62. Del Genio V, Falanga A, Allard-Vannier E, Hervé-Aubert K, Leone M, Bellavita R, et al. Design and validation of nanofibers made of self-assembled peptides to become multifunctional stimuli-sensitive nanovectors of anticancer drug doxorubicin. Pharmaceutics. 2022;14:1544. https://doi.org/10.3390/pharmaceutics14081544.
63. Sherman F. Getting started with yeast. Methods Enzymol. 1991;194:3–21. https://doi.org/10.1016/0076-6879(91)94004-v.
64. Vitale S, Di Pietro A, Turra D. Autocrine pheromone signalling regulates community behaviour in the fungal pathogen *Fusarium oxysporum*. Nat Microbiol. 2019;4:1443–9. https://doi.org/10.1038/s41564-019-0456-z.
65. Rodríguez-Moraga N, Ramos-Martín F, Buchoux S, Rippa S, D'Amelio N, Sarazi C. The effect of rhamnolipids on fungal membrane models as described by their interactions with phospholipids and sterols: an in silico study. Front Chem. 2023;11:1124129. https://doi.org/10.3389/fchem.2023.1124129.
66. Barra T, Falanga A, Bellavita R, Laforgia V, Prisco M, Galdiero S, et al. GH625-liposomes deliver PACAP through a dynamic in vitro model of the blood-brain barrier. Front Physiol. 2022;13:932099. https://doi.org/10.3389/fphys.2022.932099.
67. Bellavita R, Buommino E, Casciaro B, Merlino F, Cappiello F, Marigliano N, et al. Synthetic amphipathic β-sheet temporin-derived peptide with dual antibacterial and anti-inflammatory activities. Antibiotics (Basel). 2022;11:1285. https://doi.org/10.3390/antibiotics11101285.
68. Duzgunes N. Fluorescence assays for liposome fusion. Methods Enzymol. 2003;372:260–74. https://doi.org/10.1016/S0076-6879(03)72015-1.
69. Vitiello G, Falanga A, Petruk AA, Merlino A, Fragneto G, Paduano L, et al. Fusion of raft-like lipid bilayers operated by a membranotropic domain of the HSV-type I glycoprotein gH occurs through a cholesterol-dependent mechanism. Soft Matter. 2015;11(15):3003–16. https://doi.org/10.1039/c4sm02769h.
70. Grieco P, Carotenuto A, Auriemma L, Saviello MR, Campiglia P, Gomez-Monterrey IM, et al. The effect of d-amino acid substitution on the selectivity of temporin L towards target cells: identification of a potent anti-Candida peptide. Biochim Biophys Acta. 2013;1828(2):652–60. https://doi.org/10.1016/j.bbamem.2012.08.027.
71. Strambini GB, Gonnelli M. Fluorescence quenching of buried Trp residues by acrylamide does not require penetration of the protein fold. J Phys Chem B. 2010;114(2):1089–93. https://doi.org/10.1021/jp909567q.
72. Yamawaki Y, Yufu T, Kato T. The effect of a peptide substrate containing an unnatural branched amino acid on chymotrypsin activity. Processes. 2021;9:242. https://doi.org/10.3390/pr9020242.
73. Rispail N, Di Pietro A. *Fusarium oxysporum* Ste12 controls invasive growth and virulence downstream of the Fmk1 MAPK cascade. Mol Plant Microbe Interact. 2009;22(7):830–9. https://doi.org/10.1094/MPMI-22-7-0830.
74. Schindelin J, Arganda-Carreras I, Frise E, Kaynig V, Longair M, Pietzsch T, et al. Fiji: an open-source platform for biological-image analysis. Nat Methods. 2012;9(7):676–82. https://doi.org/10.1038/nmeth.2019.
75. Stuart MCA, van de Pas JC, Engberts JBFN. The use of Nile Red to monitor the aggregation behavior in ternary surfactant–water–organic solvent systems. J Phys Org Chem. 2005;18(9):929–34. https://doi.org/10.1002/poc.919.
76. Amdursky N, Erez Y, Huppert D. Molecular rotors: what lies behind the high sensitivity of the thioflavin-T fluorescent marker. Acc Chem Res. 2012;45(9):1548–57. https://doi.org/10.1021/ar300053p.
77. Lopez-Berges MS, Daboussi MJ, Wahab HA, Vasnier C, Roncero MI, Dufresne M, et al. Identification of virulence genes in Fusarium oxysporum f. sp. lycopersici by large-scale transposon tagging. Mol Plant Pathol. 2009;10(1):95–107. https://doi.org/10.1111/j.1364-3703.2008.00512.x.
78. Oliviero G, D'Errico S, Pinto B, Nici F, Dardano P, Rea I, et al. Self-assembly of G-rich oligonucleotides incorporating a 3'-3' inversion of polarity site: a new route towards G-wire DNA nanostructures. ChemistryOpen. 2017;6(4):599–605. https://doi.org/10.1002/open.201700024.

Publisher's Note